Aizenshtadt, A. et al. (2024) Pump-less, recirculating Organ-on-Chip (rOoC) platform to model the metabolic crosstalk between islets and liver. *Advanced Healthcare Materials*. (doi: 10.1002/adhm.202303785)

https://eprints.gla.ac.uk/311280/

Deposited on 25 January 2024

Pump-Less, Recirculating Organ-On-Chip (rOoC) Platform To Model The Metabolic Crosstalk Between Islets And Liver

Aleksandra Aizenshtadt[1, 2 §], Chencheng Wang[1, 3§], Shadab Abadpour[1, 3, 4], Pedro Duarte Menezes[1, 5], Ingrid Wilhelmsen[1, 2], Andrea Dalmao-Fernandez[1 , 6], Justyna Stokowiec[1, 2], Alexey Golovin[1, 2], Mads Johnsen[7], Thomas M. D. Combriat[1], Hanne Røberg-Larsen[1, 7], Nikolaj Gadegaard[1, 5], Hanne Scholz[1,3#], Mathias Busek[1, 2#], Stephan J.K. Krauss[1, 2#]*

⁎ Corresponding author

§ Authors contributed equally to this work.

Authors share senior authorship.

[1] Hybrid Technology Hub Centre of Excellence, Institute of Basic Medical Science, University of Oslo, P.O. Box 1110, 0317 Oslo, Norway.

[2] Dep. of Immunology and Transfusion Medicine, Oslo University Hospital, P.O. Box 4950,0424 Oslo, Norway.

[3] Dep. of Transplantation Medicine, Experimental Cell Transplantation Research Group, Oslo University Hospital, P.O. Box 4950,0424 Oslo, Norway.

[4] Institute for Surgical Research, Oslo University Hospital, Oslo, Norway

[5] James Watt School of Engineering, University of Glasgow, Rankine Building, Glasgow G12 8LT, UK

[6] Department of Pharmacy, Faculty of Mathematics and Natural Sciences, University of Oslo, P.O. Box 1083, 0316 Oslo, Norway.

[7] Section for Chemical Life Sciences, Department of Chemistry, University of Oslo, P.O. Box 1033, 0315 Oslo, Norway.

aleksandra.aizenshtadt@medisin.uio.no

Abstract

Type 2 diabetes mellitus (T2DM), obesity, and metabolic dysfunction-associated steatotic liver disease (MASLD) are epidemiologically correlated disorders with a worldwide growing

WILEY-VCH

prevalence. While the mechanisms leading to the onset and development of these conditions are not fully understood, predictive tissue representations for studying the coordinated interactions between central organs that regulate energy metabolism, particularly the liver and pancreatic islets, are needed. Here, a dual pump-less recirculating Organ-on-Chip (dual-rOoC) platform that combines human pluripotent stem cell (sc)-derived sc-liver and sc-islet organoids is presented. The platform reproduces key aspects of the metabolic cross-talk between both organs, including glucose levels and selected hormones, and supports the viability and functionality of both sc-islet and sc-liver organoids while preserving a reduced release of pro-inflammatory cytokines. In a model of metabolic disruption in response to treatment with high lipids and fructose, sc-liver organoids exhibit hallmarks of steatosis and insulin resistance, while sc-islets produce pro-inflammatory cytokines *on-chip*. Finally, the platform reproduces known effects of anti-diabetic drugs on-chip. Taken together, the platform provides a basis for functional studies of obesity, T2DM, and MASLD *on-chip*, as well as for testing potential therapeutic interventions.

List of Abbreviations

ECM	Extra-Cellular Matrix	OC	Organoid Compartment
FEM	Finite Element Method	OCR	Oxygen Consumption Rate
FFA	Free Fatty Acids	ODE	Ordinary Differential Equation
GSIS	Glucose-Stimulated Insulin Secretion	PC	Perfusion Channels
HSC	Hepatic Stellate Cell	PHH	Primary Human Hepatocytes
IC	Islet Compartment	μPIV	micro-Particle-Image-Velocimetry
IR	Insulin Resistance	SI	Secretion Index
LSEC	Liver Sinusoidal Endothelial Cell	T2DM	Type-2 Diabetes Mellitus
LC	Liver Compartment	TNF-α	Tumor Necrosis Factor-alpha
MASLD	Metabolic Dysfunction-Associated Steatotic Liver Disease		
MCP-1	Monocyte Chemoattractant		

WILEY-VCH

Protein-1

1. Introduction

The epidemiologically correlated disorders type 2 diabetes mellitus (T2DM), obesity, and metabolic dysfunction-associated steatotic liver disease/steatohepatitis (MASLD/MASH), previously known as non-alcoholic fatty liver disease/steatohepatitis (NAFLD/NASH),[1] are a worldwide disease group with steadily growing prevalence.[2] The international diabetes federation (IDF) estimated that in 2021, approximately 537 million adults were living with T2DM worldwide.[3] MASLD/MASH affects approximately 25 % to 30 % of the global population,[4] and an estimated 1 billion people worldwide are obese.[5] While the mechanisms leading to the onset and development of these conditions are not fully understood, with both genetic and lifestyle factors being explored,[6,7] recent studies have suggested a strong association between MASLD, T2DM, and obesity, whereby the risk of developing T2DM increases 5-fold in the presence of MASLD.[8] Tissues that regulate energy and metabolic homeostasis include the pancreatic islets, liver, muscles, adipose tissue, gut, and brain. Amongst these tissues, the cross-talk between pancreatic islets and the liver is centrally involved in glucose homeostasis and lipid metabolism. In this function, it fine-tunes the regulation and adaptive responses to metabolic and nutritional states through an integrated communication using protein hormones, peptides, factors, metabolites, and the cargo of extracellular vesicles, mainly miRNAs.[9]

Under physiological conditions, in response to increased blood glucose levels, beta cells in the pancreatic islets secrete insulin, which promotes glucose uptake and processing in hepatocytes. When the glucose level is reduced, alpha cells in the pancreatic islets secrete glucagon, which triggers hepatic glucose production by increased glycogenolysis and gluconeogenesis, and by decreased glycogenesis and glycolysis.[10] Both insulin and glucagon are also involved in hepatic lipid metabolism whereby insulin controls the synthesis and storage of lipids in the liver in part by increasing de novo lipogenesis, suppressing fatty acid oxidation, and promoting triglyceride esterification and secretion.[11] Glucagon promotes liver lipolysis producing glycerols and supporting amino acid catabolism, both serving as substrates for gluconeogenesis.[12] The metabolism-regulating cross-talk mediated by insulin and glucagon is complemented by a plethora of proteins secreted by the liver (hepatokines), including angiopoietin-like 8 (ANGPTL8),[13] Fetuin-A,[14] follistatin,[15] insulin-like growth factor binding proteins (IGFBP),[16,17] sex hormone-binding globulin (SHBG), fibroblast growth factor 21 (FGF21), Hepatic Growth Factor (HGF), Kisspeptins, Serpin B1, selenoprotein and others.[9]

WILEY-VCH

In MASLD, the above-described cross-talk between the liver and the pancreas is disturbed and patients show a high prevalence of insulin resistance (IR), a condition in which the body's cells become less responsive to the effects of insulin leading to increased levels of blood glucose.[18] In addition, an insufficient compensatory beta cell function in the pancreatic islets has been associated with MASLD, causing reduced levels of insulin release upon glucose stimulation.[19] Also, an elevated plasma glucagon concentration is a biochemical hallmark of T2DM, and a lower glucagon-to-insulin ratio which indicates relatively high insulin levels is associated with the presence of MASLD.[20]

Metabolic stress in both liver tissue and pancreatic islets is closely interlinked with inflammation and can trigger the release of pro-inflammatory cytokines. In the liver, the release of interleukin-1 beta (IL-1β) is mainly regulated by metabolic stress and acts as a primary inflammatory cytokine that recruits downstream pro-inflammatory mediators.[21] One such mediator, interleukin-6 (IL-6), regulates non-oxidative glucose metabolism and increases plasma levels of triglycerides. Strategies for decreasing the effect of IL-6, e.g. by anti-IL-6 antibodies, show a positive effect on insulin resistance.[22] Another important cytokine that is regulated by IL-1β is the tumor necrosis factor-alpha (TNF-α).[23] TNF-α has been shown to correlate with IR in diabetic patients and is also seen as a main causative factor for the development of IR in rodent models.[24,25] Monocyte chemoattractant protein-1 (MCP-1), a chemokine produced by islets, is a further central component in metabolic stress-related inflammation. Its production is affected by the primary inflammatory cytokines IL-1β and TNF-α. Upon IR, excessive MCP-1 production by the islets perpetuates the cycle of inflammation and, correspondingly, a low level of MCP-1 is seen as the most relevant factor for functional islet health upon transplantations.[26] Likewise, a high level of the pro-inflammatory cytokine interferon-γ-induced protein 10 (IP-10), also produced by islets, has been shown to correlate with poor islet transplant outcomes.[27]

Until now, human clinical studies[28,29] and animal models[30–32] have been used to study the onset and progression of obesity, T2DM, and MASLD, as well as the impact of drug candidates on these conditions. Recently, human micro-physiological models, including liver and pancreas models, have been developed that allow micro-dissecting aspects of the metabolic cross-talk between both. Such models can accelerate our understanding of MASLD and serve as a preclinical model for drug design and testing.[33]

An important development for micro-physiological systems that model organ function and cross-talk is organoid technology. Recently, islet and liver organoids derived from patients or grown from pluripotent stem cells (PSC) became available.[34] A metabolic cross-talk between these different can be modeled using Organ-on-Chip (OoC) technology that combines tissue

WILEY-VCH

and micro engineering.[35] In a pioneering study, co-culture of human pancreatic islet micro-tissues and liver spheroids was done in a Transwell-based OoC platform.[36] A more advanced system was subsequently used to model and predict in silico glucose metabolism *on-chip*.[37] Subsequent co-culture examples encompass i) a modular multi-tissue chip device that displays a counter-regulatory transcriptional process between primary human liver spheroids and intact primary human islets combined *on-chip*,[38] and ii) co-culture of liver and islet organoids derived from human, induced pluripotent stem cells, which enabled glucose-triggered insulin release from islet organoids and enhanced glucose consumption in liver organoids.[39] While these models show an impressive advance in coupling islets and liver *on-chip*, allowing functional readouts and in the case of the sc-derived islets and liver organoids a 30-day co-culture, the current models rely on pump-driven systems. However, a major disadvantage of pump-driven OoC systems is their low scalability and usability,[40] as well as an unphysiological high media-to-cell ratio and surface area which increases the risk of surface binding of proteins such as insulin.[41]

Here we present a novel scalable OoC format, termed dual pump-less recirculating Organ-on-Chip (dual-rOoC), that has been adapted to support long-term functional co-culture of human pluripotent stem cell (hPSC)-derived pancreatic islet organoids (sc-islets) and liver organoids (sc-liver). The platform was developed based on the recently published rOoC platform that generates a directional, gravity-driven flow,[42] however, with the integration of two gravity-driven circuits, separated by a membrane that allows the micro-dissection of the circuits containing islet organoids and liver organoids respectively, while permitting the transport of proteins, glucose, and other small molecules between the circuits. The platform enabled the functional co-culture of hPSC-derived sc-islet and sc-liver organoids for at least 2 weeks with stable viability and functionality of both organoids. An improved glucose-stimulated insulin secretion (GSIS) by the islets and insulin/glucose consumption by liver organoids demonstrated that the platform enables successful functional and supportive cross-talk between islets and liver organoids. Supplementation of culture medium with free fatty acids (FFA) and fructose, mimicking an unhealthy diet, caused significant changes in the morphology, metabolism, and functionality of both organ mimics, alongside increased levels of pro-inflammatory cytokine secretion, including IL-6, IL-8, IL-22, and MCP-1. Tests with the three drugs metformin, tolbutamide, and pyruvate kinase activator allowed micro-dissecting drug responses in the sc-islet and sc-liver circuits and established the validity of the platform for drug testing.

2. Results

2.1. Dual-rOoC platform design, fabrication, and characterization

Recently, we introduced the rOoC platform concept that combines the possibility of recirculating cell media in a microfluidic platform with high scalability and flexibility.[42] The published system contained two nested fluidic circuits, separated by two organoid compartments (Loop-in-Loop layout). Each fluidic circuit was built up by two elongated reservoirs that were connected by two perfusion channels (PCs). The Loop-in-Loop layout is well suited to cultivate liver organoids, endothelial cells, and circulating immune cells, and can be used to co-culture two types of organoids or organ mimics. However, the layout does not allow for differentially tracking the secretome, including protein hormones and metabolites, of two (different) organoids *on-chip,* nor does it allow for controlling the directionality and kinetics of protein and metabolite communication between the organoids. This is of importance when studying the cross-talk between sc-liver and sc-islets. In most published systems, directionality in the communication between organoid systems is achieved by directed flow-through perfusion, e.g. from the islet to the liver organoids,[39] but this configuration does not allow feedback back from the liver to the islet organoids, which is central in the regulation of energy homeostasis. To allow both, a bi-directional cross-talk between islet and liver organoids with a delayed protein transport kinetics that is enhanced in one direction combined with the benefits of the rOoC platform, we designed a platform comprising two separate loops that are connected by a membrane that allows slow protein and metabolite exchange. The platform was termed dual-rOoC (Figure 1a, Figure S2a). In the dual-rOoC, one circuit was designed to contain the insulin-producing sc-islet organoids placed in the islet compartment (Figure 1a, Figure S2a, b), whereas the other circuit was designed to contain the sc-liver organoids placed in the liver compartment (Figure 1a, Figure S2a, b), which consume insulin. On the outermost right side of the liver compartment, a drainage channel was added from which media can be sampled that had passed the compartment containing sc-liver organoids. By introducing a membrane between both the islet and the liver circuit, we were able to influence the kinetics and directionality of the protein exchange between both circuits while being able to segregate and hence analyze the protein release of each organoid compartment, a feature that showed to be in particular important for studying cytokine secretion of sc-islets vs sc-liver organoids under different conditions. The fluid actuation was based on a combination of specifically designed reservoirs and PCs combined with a 3D-tilting/rotating platform to produce a directed re-circulating flow without the need for pumps. Please refer to the previously published paper for a detailed description of this process.[42] Suppl. Video V1 exemplifies the process.

In the dual-rOoC platform, the PC dimensions were chosen to be of the sizes of smaller arteries in the body[43] and are between 1 and 2 mm wide and 0.5 or 0.9 mm high. To have a media-to-cell ratio comparable to standard cell culture plastics (96/48 well plates), we selected a reservoir volume of 300 µL. The organoid chambers (OCs) were designed in two different configurations: for sc-liver organoids, we used the previously described stepped channel

geometry with a reduced channel height of 500 µm between the OC and the PC (Figure 1c) bordering 900 µm high PCs.[42] In this configuration, the ECM was retained in the OC due to capillary forces and did not spill into the PC. The length of the liver compartment (LC) was set to 4 mm so that 10-20 sc-liver organoids could be embedded in an ECM (Geltrex, ThermoFisher Scientific), a condition that allowed them to retain viability and functionality over the tested period of 14 days (see Figure S2). While this configuration was well suited for sc-liver organoids, the same configuration showed a reduced viability of sc-islet organoids which we rationalized to be caused by insufficient nutrient and oxygen supply due to the small exchange area between the PCs and the OC. To increase the nutrient exchange area, we applied a modified version of the OC termed islet compartment (IC). In the IC, the PC and OC were stacked horizontally rather than vertically (Figure 1d). That means the PC was placed on top of the IC so that nutrients could be exchanged over the full width of the channel between the ECM-embedded sc-islet organoids (3-10 sc-islets per IC) and PC. In order to prevent the ECM from blocking the PC on top, a window with a slightly decreased width was placed between the IC and the PC.
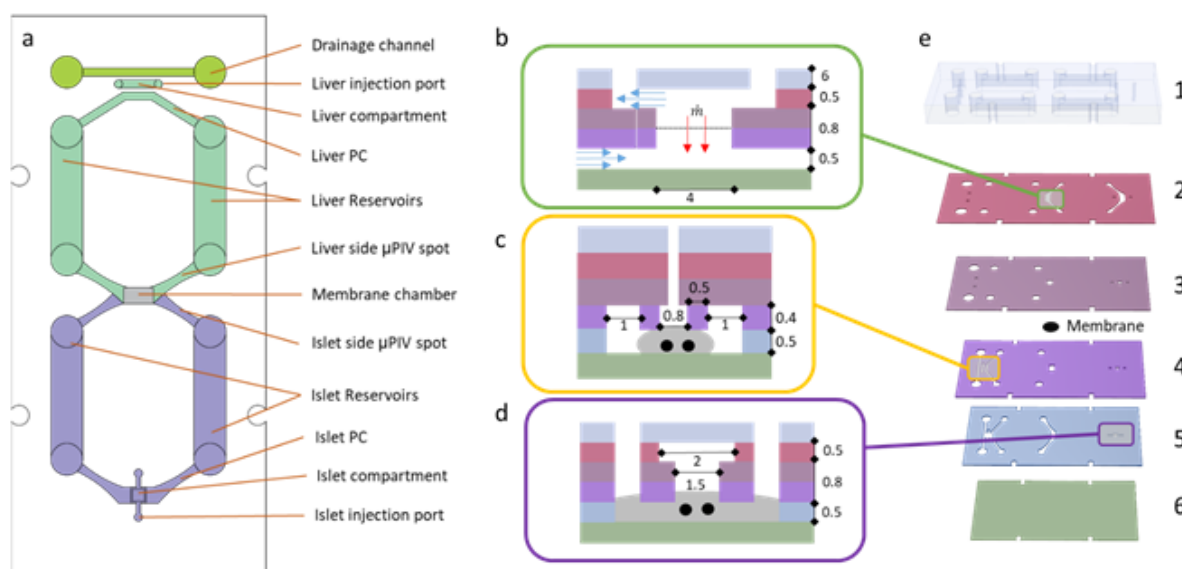
Figure 1. Principle layout of the dual-rOoC. a) Different circuits and elements of the dual-rOoC as top-view; b) Cross-section of the membrane chamber with the separated top and bottom flow (blue arrows) and red arrows indicating trans-membrane flow; c) & d) Cross-section of the liver & islet compartment with organoids indicated as black dots and the ECM marked in grey; e) Explosion-view of the full device consisting of 6 layers. All dimensions are given in mm.

The multilayer fabrication process for the rOoC platform has been described earlier and is detailed in the methods part.[44] The dual-rOoC is composed of 6 Poly(methyl methacrylate) (PMMA) layers with varying thickness (Figure 1e):

1. Layer: (6 mm) Contains the laser-engraved reservoirs and cell injection ports to load the organoids into the IC and LC.
2. Layer: (0.5 mm) Includes PCs at the islet loop and through holes to the next layers.
3. Layer: (0.4 mm) Includes the connecting windows for the IC and the membrane and through holes to the next layers.
4. Layer: (0.4 mm) Contains the same windows and connecting holes as layer (3) as well as the LC, PCs of the liver side, and drainage channels to sample media from the liver organoids.
5. Layer: (0.5 mm) Includes the LC, IC, drainage channels, and the rest of the liver PCs.
6. Layer: (0.175 mm) Is the sealing layer and allows on-chip confocal imaging.

Together, layers 3, 4, 5, and 6 form a stepped channel layout (Figure 1c/d) that prevents the ECM (grey) from entering the PCs.[45] Due to capillary forces, the liquid ECM is retained in the region where the channel dimension is abruptly changed and the organoids (black) are fixed in place. Using this layout, a biodegradable separation layer[46] is formed between the OCs (LC and IC) and the PCs allowing for spatial defining of the cell composition.[45]

To control peptide and metabolite exchange between the two loops of the dual-rOoC, a permeable membrane was sandwiched between layers 3 and 4 during the thermal bonding (Figure 1b). To prevent leakage between the layers and the membrane, a 4 x 2 mm^2 window was introduced between both layers preventing that media bypasses the membrane when it is slightly deflected during the bonding process.

2.2. Flow characterization and modeling of fluidics in and between the loops.

Nutrients, metabolites, and proteins such as insulin are transported via diffusion and advection within the dual-rOoC. A general mathematic description for the transport of a component with the concentration c is given by the advection-diffusion equation:

$$\frac{\delta c}{\delta t} = \nabla \cdot (D \nabla c) - \nabla \cdot (\vec{v} c) + R \tag{1}$$

The first term denotes the diffusive substance transport with a given diffusion constant D, and the second part of the equation is the advective transport given the flow vector field $\vec{v}$ and R denotes the reactive term (e.g. the consumption/metabolism reaction). Advective processes are mainly responsible for the mass transport in the reservoirs and PCs whereas diffusion is the main driver for transport processes at the membrane and within the OCs.

The tilting motion induces a discontinuous flow in the PCs that can be measured with micro-particle-image-velocimetry (µPIV) by tracking the displacement of microparticles dispensed into the media.[47] The experimental setup is detailed in the previous paper and the methods

section.[42] The flow rate in the dual-rOoC was measured in the respective out- and inlets of the membrane compartment at the sc-islet and the sc-liver side (Figure 1a). The time-dependent flow rate $Q(t)$ was calculated from the average flow velocity $\bar{v}$ given the channel cross section (h, w) and a calibration factor k:

$$Q = \bar{v} \cdot k \cdot w \cdot h \tag{2}$$

The calibration factor is required because the tracked particles in the observed channel area are traveling in different focal planes with different speeds because of the parabolic velocity profile in the z-direction and the fact that the optical setup records different focal plains due to the low magnification used. The calibration process is detailed in the methods part. We measured a calibration factor of: $k \approx 1.84$.

Flow-time-curves as well as the transported volume $V(t) = \int Q\,dt$ are plotted in Figure 2a. The Python script used to plot the data is given in the Suppl. Material. To obtain a directed flow, only one of the reservoirs in each circuit should be filled with a volume V_{res}, and this volume is fully transported during one rotation (see Suppl. Video). Thus, the average flow rate should be dependent only on the rotation frequency f in rpm:

$$Q = V_{res} \cdot {}^{f}\!/_{60} \tag{3}$$

For a total volume of 300 µL, this is valid for the flow-curve obtained in the islet-PC. The transported volume for one rotation equals 269 µL (mean flow rate 13.45 µL s^{-1}). This value is lower than the total volume because the total circulating volume is subtracted from the channel volume ($Vc \approx 40\mu L$ for islet PC). A significant difference is visible for the liver-PC where the transported volume is only 150 µL whereas the channel volume is <100 µL. That means that the transported volume is at least 50 µL less than expected. A possible explanation for this difference is an asymmetry between the fluidic resistances for both PCs on the liver side. The PCs at the side of the LC have a cross section of 0.9 x 1 mm^2 whereas the PCs connecting the membrane with the reservoirs are only 0.5 x 1 mm^2. This asymmetry will lead to a significantly increased (bi-directional) volume transport near the LC whereas the flow rate at the membrane is only 7.67 µL s^{-1}.

A two-dimensional (2D) finite element method (FEM) model has been developed using COMSOL Multiphysics (COMSOL, Stockholm, Sweden) version 6.0 to simulate the dynamics of flow and mass transport (Eq. 1) associated with the membrane interface of the device. From the library of available modules, the "Porous Media Flow" and "Transport of Diluted Species" modules were selected. The purpose of the first module is twofold. First, it employs the Navier Stokes and Continuity equations to solve for the laminar free flow of media along the channels,

by ensuring the conservation of momentum and mass respectively.[48] Second, it engages Darcy's Law to simulate the flow of media across the membrane, treated as a porous medium. The underlying equations are given in the Materials and Methods section. The transient flow behavior was simulated by concatenating analytical functions towards better replicating the flow-time-curves measured experimentally (Figure 2a) for each channel (Figure S1a/b). The flux of molecules too, was defined to follow the same convection pattern. The whole model is shown in Figure 2c. In contrast to the closed loop structure from Figure 1, the model is simplified to two channels connected to an up- and a downstream reservoir. However, a "continuous" boundary condition (orange line in Figure 2c) is set at each reservoir outlet, meaning that every molecule leaving the respective reservoir is added to the opposite reservoir. The donor channel is defined to provide a continuous supply of insulin molecules and has an initial concentration of c_0 (green lines in Figure 2c). The acceptor channel is filled with an initial concentration of 0 and the average insulin concentration at the acceptor side (c_2) is calculated. The underlying parameter set is given in Table 1 and membrane chamber dimensions are given in Figure 1b.

Table 1: Parameters used for mass transport modeling and insulin transport experiments

Parameter Family	Parameter	Value
Membrane	Porosity [%]	11.3
	Pore radius [μm]	3
	Thickness [μm]	22
Channel widths	Membrane chamber width [mm]	2
	Islet-PC width [mm]	1.1
	Liver-PC width [mm]	1
Reservoirs	Islet circuit volume [μL]	450
	Liver circuit volume [μL]	375
Flow conditions	Max. platform tilt [°]	18
	Tilting speed [rpm]	3
	Media volume in each circuit [μL]	300
	Initial concentration [μM]	0.58

Chemical properties and conditions		
	Diffusion coefficient insulin [m^2 s^{-1}]	1.5e-10
Test conditions	Temperature [°C]	37
	Density of water at 37 °C [kg $(m^3)^{-1}$]	993.3
	Dynamic viscosity of water at 37 °C [mPa*s]	0.6913

The first part of the model yields the velocity profile over time. An example is given in Figure 2d. In Figure S1c, the flow profile is given for 4 different time points of one full revolution at 3 rpm. As it is visible, the flow pattern is alternating between the islet- and liver-PC with a maximum velocity at the islet-PC occurring at 15 s, almost no flow on both sides around 0 s and 10 s, and a maximum flow in the liver-PC at 5 s. This alternating flow pattern induces a transient mass flux $\dot{m}(t)$ through the membrane which is driven by the pressure difference between both circuits. In Figure 2e, the acceptor concentration c_2 normed to the initial concentration c_0 is plotted as a color plot 20 s after starting the simulation. It becomes obvious that insulin is transported to the outlets. In Figure S1d/e color plots are given for different time points to indicate the transient behavior. Within 60 minutes (min), the concentration ratio c_2/c_0 converges to 1 (Figure 2f). The speed of equalization is different for both the transport from top to bottom and vice versa (red/blue curve). This data is in good alignment with the experimentally obtained data sampled every 5 min at the acceptor/donor side (insulin concentration in each circuit was measured using ELISA).

A simplified model can be obtained by setting up the mass balance in both reservoirs (donor: V_1, acceptor: V_2):

$$c_1(t) = \frac{(m_0 - \int_0^t \dot{m}\,dt)}{V_1} \qquad c_2(t) = \frac{\int_0^t \dot{m}\,dt}{V_2} \qquad (4)$$

WILEY-VCH
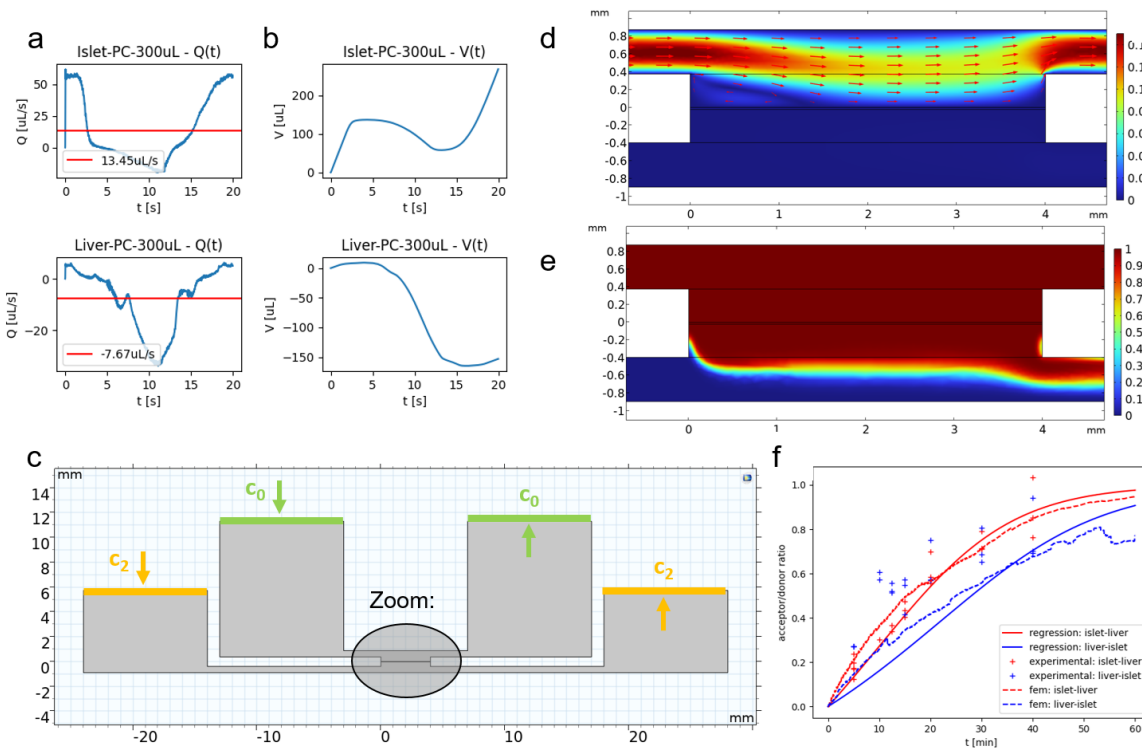
Figure 2: Modelling and technical characterization of the dual-rOoC. a) Measured velocity-time curves obtained at the positions indicated in Figure 1a with a tilt of 18°, a speed of 3 rpm, and a total volume of 300 µL. The red line indicates the mean flow rate; **b)** Transported volume obtained by integrating a); **c)** Model description (cross-section) indicating the two reservoirs and the exchange membrane in the middle. The green lines indicate the fixed concentration boundary condition at the donor side and the orange line indicates the continuous boundary condition with all molecules leaving the system to the right and reentering the reservoir to the left; **d)** Flow profile at the sc-islet-PC (top) and the sc-liver-PC (bottom) (zoomed area of c). The red arrows indicate the flow velocity field; **e)** Color plots of the insulin concentration ratio c_2/c_0 distribution for the islet-PC (top) as donor and the liver-PC (btm) as acceptor channel; **f)** Insulin concentration ratio c_2/c_0 for the transport from the islet to the liver circuit (red) and vice versa (blue). The crosses indicate measured values (donor concentration: 2µg mL^{-1}, n=2 replicates), the dashed line is the result obtained via the Comsol model and the continuous line is the result obtained via regression and solving the ODE from eg. 6.

This time, with a variable donor concentration c_1 that depends on the initial mass of insulin m_0 diluted in V_1. The mass flux $\dot{m}(t)$ depends on c_1, c_2 and $\dot{m}_{max}$ is the max mass flux for $c_1=c_0$ and $c_2=0$:

$$\dot{m}(t) = \dot{m}_{max}(1 - {c_2(t)}/{c_1(t)}) \tag{5}$$

Together with Eq. 4, this yields the following ordinary differential equation (ODE) for the mass flow:

$$\left. m(t) \middle/ \dot{m}_{max} \right. = 1 - \left. V_1 \middle/ V_2 \right. \left[\left. m(t) \middle/ (m_0 - m(t)) \right. \right] \tag{6}$$

The ODE is solved using the Python script in the Suppl. Material and the parameters from Table 1. Via regression, maximum mass fluxes for the transport from the islet- to the liver-PC $\dot{m}_{isl-liv} \approx 0.16$, and vice versa $\dot{m}_{liv-isl} \approx 0.11$ had been obtained (see Figure 2f).

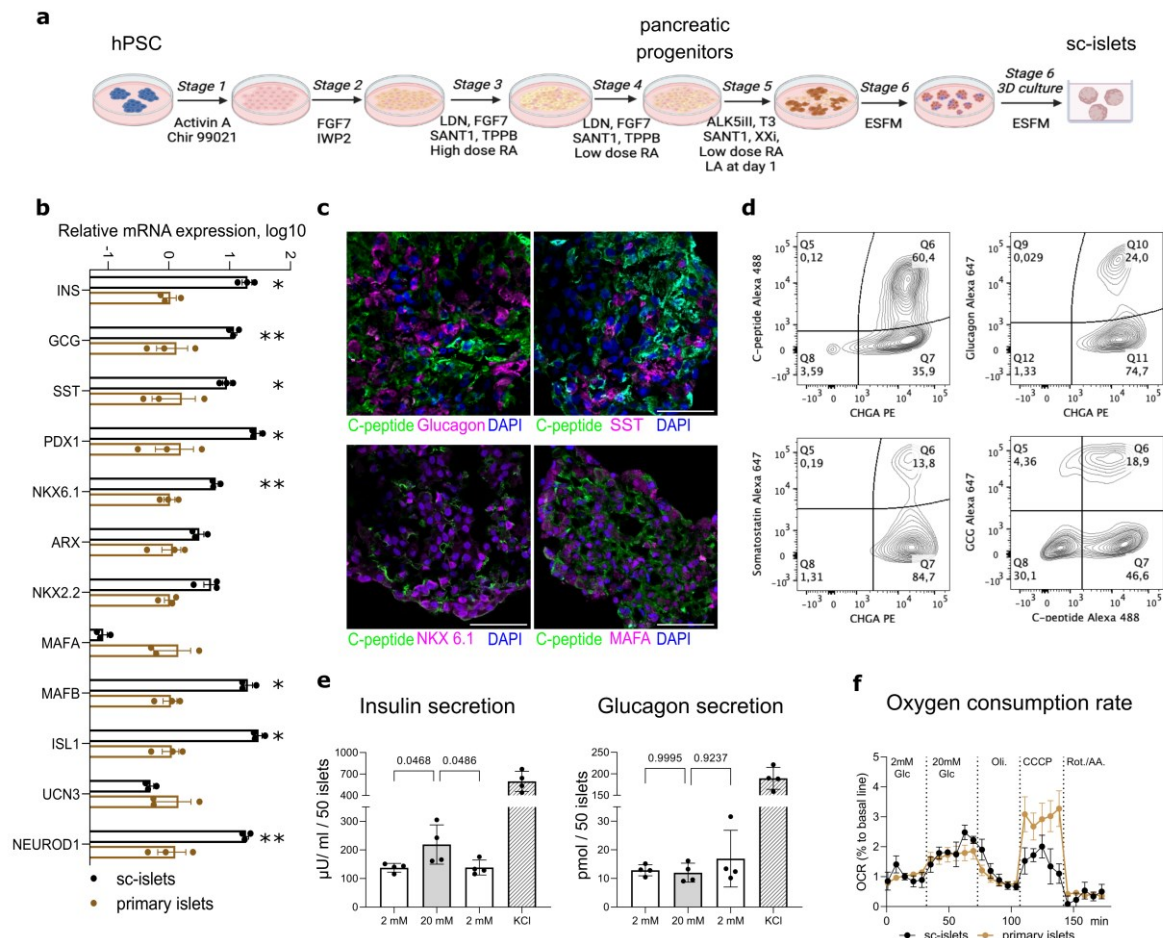## 2.3. Generation of sc-islet organoids and sc-liver organoids

To establish an *in vitro* model of the islets-liver metabolic axis on the dual-rOoC chip platform, human embryonic stem cells (hESC; line H1) were differentiated to sc-islet and sc-liver organoids using modified lineage-specific differentiation protocols (Figure 3a and Figure 4a).

Sc-islet organoids were generated according to a previously published 6-stage differentiation protocol[41,49] (Figure 3a) as described in the Materials and Methods section. Gene expression analysis of the sc-islets (Figure 3b) demonstrated the expression of key signature genes for α- β- and γ-cells in the organoids. When benchmarked to patient-derived primary adult islets, sc-islet organoids were characterized by higher expression levels of the genes for insulin and glucagon, as well as for the transcription factors pancreatic and duodenal homeobox 1 *(PDX1)*, musculoaponeurotic fibrosarcoma oncogene homolog b *(MAFB)* and neurogenic differentiation 1 *(NEUROD1)*, while the expression of the *MAF BZIP Transcription Factor A (MAFA)* – a transcription factor specific for mature β-cells[50] – was lower in sc-islet organoids compared to primary islets. Immunofluorescent imaging confirmed the presence of insulin-, glucagon- and somatostatin-positive cells, as well as the expression of endocrine-specific transcription factors MAFA and NKX6.1, both markers for islet β-cells (Figure 3c). The cell composition of the generated sc-islets was analyzed using flow cytometry (Figure 3d). More than 90 % of the cells were chromogranin A (CHGA)-positive endocrine cells, in which >60 % of the cells were insulin-positive β-like cells (C-peptide, Alexa 488), >20 % of the cells were glucagon-positive α-like cells (glucagon, Alexa 647), while >10 % of the cells were somatostatin-positive δ-like cells (somatostatin, Alexa 647). In addition, about 20 % insulin and glucagon double positive cells were observed in the sc-islet organoids indicating a certain degree of sc-islets immaturity (C-peptide, Alexa 488/GCG, Alexa 647).

Next, the functionality of the sc-islet organoids was tested. Secretion of insulin upon glucose stimulation is a crucial functional hallmark for β-like cells within sc-islets. A significant increase in insulin secretion from the sc-islets was found in response to high glucose stimulation (20 mM glucose) with a secretion index (SI) of ~1.57. The insulin secretion did normalize upon reduction to 2 mM glucose (Figure 3e).

Moreover, we detected the secretion of glucagon by sc-islet organoids, demonstrating the functionality of α-like cells within the sc-islet organoids. Although high glucose stimulation did not significantly modulate the glucagon secretion (SI = 0.94), we observed a moderately increased secretion of glucagon in response to lowering the glucose concentration (from 20 mm to 2 mm; SI=1.35) (Figure 3e), partially resembling physiological glucose-dependent glucagon secretion. Maximal glucagon and insulin secretion were observed upon exposure to potassium chloride (KCl), as expected.

Adequate hormone secretion in response to changes in glucose concentrations requires metabolic maturity and functional mitochondria in endocrine cells.[51,52] To validate the mitochondrial capacity of the generated sc-islet organoids, we analyzed glucose-stimulated mitochondrial respiration in sc-islets in comparison to donor-derived islets. For this we analyzed the cellular oxygen consumption rate (OCR) in response to a 20 mm glucose challenge, followed by the application of the ATP synthase inhibitor Oligomycin A (ATP-synthase-driven OCR) and the uncoupling agent carbonyl cyanide carbonyl cyanide 388 3-chlorophenylhydrazone (CCCP, maximal OCR capacity). Similar to primary adult islets, the sc-islet organoids exhibited an increased oxygen consumption upon 20 mm glucose stimulation, and were characterized by a maximal respiration capacity (CCCP-stimulated OCR) approaching the level of human primary islets (Figure 3f).

Figure 3. Generation and characterization of sc-islet organoids from human pluripotent stem cells (hPSC). *a) Scheme of the differentiation protocol; b) Comparison of gene expression between sc-islet organoids (n = 3 independent differentiations) and primary adult islets (n = 3 donors). INS: insulin, GCG: glucagon. Significance was calculated using multiple unpaired t-tests, * p < 0,05, ** p < 0,01; c) Representative confocal images of sc-islet organoid cryosections, labeled with antibodies against human insulin, glucagon, somatostatin (SST), NKX6.1, MAFA and nuclei (DAPI); d) Representative flow cytometry density plots showing the percentage of chromogranin A (CHGA), C-peptide, somatostatin and glucagon-positive cells, as well as C-peptide and glucagon double-positive cells in sc-islet organoids; e) Insulin and glucagon secretion by sc-islets in response to glucose stimulation and potassium chloride (KCl) (n = 3 independent differentiations). Significance was calculated using one-way ANOVA; f) glucose-stimulated mitochondrial capacity in sc-islet organoids and primary islets (n = 4 replicates for each group).*

Sc-liver organoids were generated using a previously published 10-step protocol,[53,54] which includes an aggregation step at the stage of hepatic progenitors, ensuring the formation of

uniform-size organoids of 150-200 μm (Figure 4a). Sc-liver organoids were benchmarked to freshly thawed primary human hepatocytes (PHH) characterized by the expression of hepatocytes-specific markers including hepatocyte nuclear factor 4 alpha (*HNF4a*), genes involved in glucose metabolism including glucose transporter 2 (*GLUT2),* glucose-6-phosphatase, catalytic subunit *(G6PC)*, and cytochrome P450 genes including *CYP3A4, CYP2B6* and *CYP2C9* (Figure 4b). Furthermore, the presence of non-parenchymal cells in sc-liver organoids was shown by the expression of platelet and endothelial cell adhesion molecule 1 *(PECAM-1*) as well as lymphatic vessel endothelial hyaluronan receptor (*LYVE*), present on liver sinusoid endothelial cells (LSEC), and by the expression of platelet-derived growth factor receptor (*PDGFR*), indicating the presence of stem cell-derived hepatic stellate cells. Whole-organoid immunofluorescence staining confirmed the expression of HNF4α, Albumin, CYP3A4, and alpha-1 antitrypsin (A1AT), all characteristic markers of hepatocytes (Figure 4c). In addition, the presence of both adherens junction protein E-cadherin and tight junction protein zonula occludens-1 (ZO-1), necessary for bile canaliculi formation, was confirmed. Moreover, the presence of platelet-derived growth factor receptor β (PDGFR-β), a marker for hepatic stellate cells, was seen in cells lining the inner surface of the sc-liver organoids as shown by an orthogonal view of the organoids imaged as Z-stack (Figure 4c).

Next, the functionality of sc-liver organoids was benchmarked to PHH spheroids by quantifying the production of albumin and urea (5 days of culture) (Figure 4d), followed by testing the basal and drug-induced cytochrome P450 activity (CYP1A2, CYP2C9, CYP3A4) using luciferase-based assays in the sc-liver organoids (Figure 4d). Sc-liver organoids produce both albumin and urea and demonstrated the presence of basal and inducible CYP activity.

To evaluate the ability of sc-liver organoids to develop hepatic steatosis, an initial stage of MASLD, sc-liver organoids were exposed for 5 days to a cocktail of FFA (oleic and palmitic fatty acids, 250 μm, 1:1 ratio) and fructose (10 mm). Following our previous results,[55] the incubation of the sc-liver organoids with FFA and fructose-induced an extensive accumulation of lipid droplets in the liver organoids (Figure 4e), a characteristic of MASLD. Under these conditions, sc-liver organoids demonstrated an absence of insulin-stimulated increase of glucose uptake and storage, as demonstrated by a radioactive substrate oxidation assay (Figure 4f).

Overall, the data confirmed that sc-islet organoids and sc-liver organoids generated by our protocols recapitulate main tissue-specific characteristics and functionalities at the level close to, or similar to, adult benchmark tissue. This, together with the suitability of the protocols to generate a sufficient number of organoids, allowed using the sc-islet and sc-liver organoids in the model of metabolic cross-talk healthy and diseased conditions.

WILEY-VCH

17

WILEY-VCH
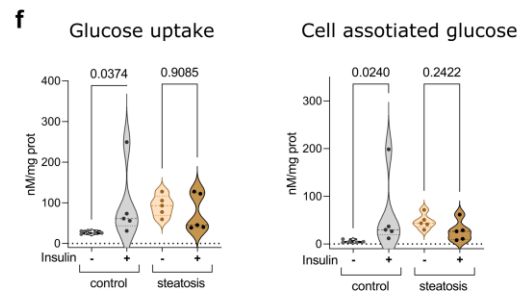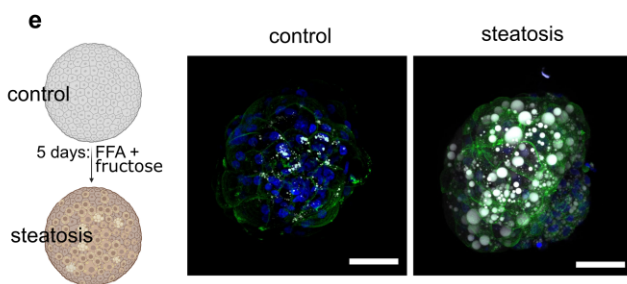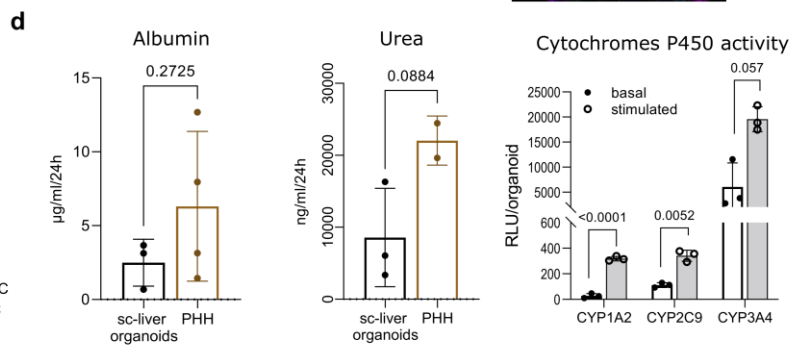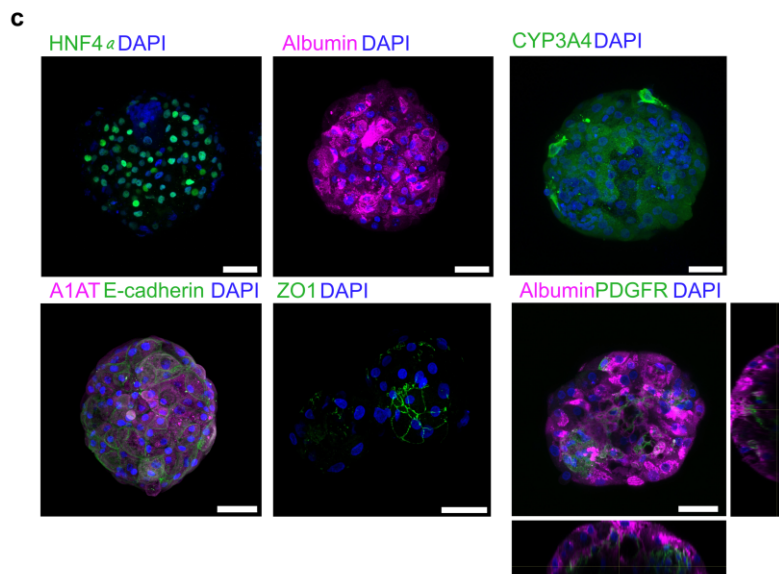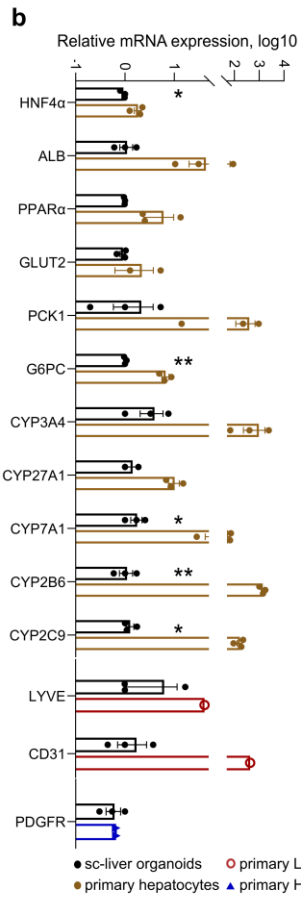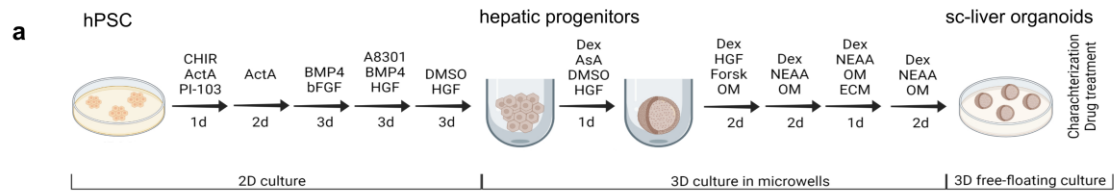
Figure 4. Generation and characterization of sc-liver organoids*. a) Scheme of differentiation protocol; b) Comparison of gene expression levels between sc-islet organoids (n = 3 independent differentiation) and PHH spheroids (n = 3 donors), primary human LSEC (n = 1 donor) and HSC (n = 2 donors), 0 h culture. Significance was calculated using multiple unpaired t-tests, * p < 0,05, ** p < 0,01; c) Representative confocal images of sc-liver organoids labeled with antibodies against HNF4α, albumin, CYP3A4, ZO1, α1-antitrypsin (A1AT), E-cadherin, nuclei (DAPI) and PDGFR-β. Scale bar 50 µm; d) Albumin and urea secretion by sc-liver organoids (sc-liver organoids from n = 3 independent differentiation) in comparison to primary human hepatic spheroids, 5 days of culture (PHH from n = 4 donors for albumin secretion and PHH from n = 2 donors for the urea secretion assay). Significance was calculated using an unpaired t-test and Mann-Whitney test correspondingly; Cytochrome P450 activity was measured in basal conditions and after 24 h of stimulation with omeprazole (50µM, for CYP1A2) or rifampicin (10µM, for CYP2C9 and CYP3A4). Significance was calculated using multiple unpaired t-tests. e) Hepatic steatosis model using sc-liver organoids in response to treatment with oleic and palmitic acids (250 µM each, 1:1) in combination with fructose (10 mM). Confocal imaging shows lipids accumulation in steatotic organoids (white – lipid droplets stained with Nile red, green – E-cadherin), scale bar 50 µm; f) Basal and insulin-stimulated glucose uptake and accumulation in sc-liver organoids under control and steatosis-inducing conditions using substrate oxidation assay with D-[^{14}C (U]glucose (0.5 µCimL^{-1}, 200 µM). Significance was calculated using one-way ANOVA on ranks (n = 5 replicates).*

2.4. Coupling of sc-islets and sc-liver organoids *on-chip*

Modeling the metabolic cross-talk between islets and liver *on-chip* (Figure 5a) requires stable long-term viability and functionality of both tissue representations. Unlike culture conditions in other platforms,[36,38,39] in the dual-rOoC, both organoid types were embedded in an ECM to provide a microenvironment that stabilizes the organoids and provides a supportive matrix.[42,56] The viability and functionality of the sc-islet and sc-liver organoids were first evaluated as mono-cultures *on-chip,* followed by combining both organoids *on-chip* using compatible media conditions. Importantly, in mono-cultures, the growth medium for the liver had to be supplemented with insulin at a concentration of 1.7 nM. In contrast, the medium for co-culture experiments did not include insulin supplements, as the insulin required for sc-liver organoids was directly supplied by the sc-islets *on-chip,* creating a sc-islet-dependent sc-liver organoid culture system. To minimize side effects of the medium on both sc-islets and sc-liver organoids, glucocorticoids had to be excluded,[57,58] which are often used for the maturation of sc-derived hepatocytes[59–62] and primary hepatocyte cultures[63,64]. Using the above culture conditions (termed co-culture medium; see Materials and Methods section), we observed high viability of both sc-islet and sc-liver organoids over 14 days in static conditions (organoids kept in a standard multiwell dish) as well as in perfused *on-chip* mono- and co-culture experiments. The viability was measured by the ATP content (Figure 5b) and visualized by Live/Dead staining (Figure S2c). Under these media conditions, both organoid types

demonstrated overall stable morphology and an expression of tissue-specific markers such as C-peptide and CYP3A4 as shown by confocal imaging *on-chip* (Figure 5c, Figure S2d).

The eliminated need for insulin in the co-culture medium already indicated that the sc-islets functionally supported the sc-liver organoids *on-chip*. To further evaluate the metabolic sc-islets/sc-liver cross-talk, we analyzed glucose-dependent insulin secretion by sc-islets and insulin consumption by sc-liver organoids in a GSIS assay. This was possible by the design of the dual-rOoC chip that allows the segregation of both circuits due to a delayed permeability of metabolites and proteins through the separating membrane.

The GSIS assay was performed on the same devices after 1 day (24 hours) and 14 days of culture with the following conditions: co-culture *on-chip* in the dual-rOoC, mono-culture *on-chip* with a liver compartment filled only with EM hydrogel, and static culture in a multiwell dish (Figure 5d). On the dual-rOoC platform, sc-islets in co-culture with sc-liver organoids showed stable insulin secretion in response to glucose stimulation over the whole culture period. In mono-culture *on-chip* and under static conditions, there was a trend for deteration of insulin secretion by the sc-islets over time in part of experiments, however not statistically significant (Figure 5d).

The insulin consumption rate (R) by sc-liver organoids in the co-culture system was determined (Figure 5e) by monitoring the insulin concentration in the sc-islets circuit and in the sc-liver drainage channel (see Figure 1a) after 1 hour of exposure to 20 mM glucose (during GSIS assay). The insulin consumption is calculated as follows:

$$R[\%] = 100 \cdot \left({c_{islet} - c_{liver}}/{c_{islet}} \right) \tag{7}$$

The mean insulin consumption by sc-liver organoids was calculated to be 84.53 % and 73.83 % at the start and by the end of co-culture, correspondingly (Figure 5e). When sc-islets were grown in *on-chip* without insulin-consuming sc-liver organoids, the loss of insulin was 25.6 % (mean value). The 25.6 % depletion of insulin in the sc-islets mono-culture is most likely explained by the adsorption of insulin to the walls of the dual-rOoC, the membrane, and the ECM in the LC, and was termed system adsorption (Figure 5e).

As glucose uptake is the main hepatic response to insulin stimulation, the glucose levels in the culture medium were evaluated at the beginning of the co-culture (day 1) and after 14 days (24 hours after the last media change). The co-culture medium contains 8.3 mM glucose at the start. During the whole co-culture period, the glucose concentration in the dual-rOoC remained within the range between 5 and 7 mM, which is close to the physiological range in human blood (termed euglycemia) (Figure 5f). Glucagon secretion by the sc-islets was confirmed during the

whole period of the co-culture with an average of 50-60 pmol which compares to a physiological range of 20-40 pmol (Figure 5g). Glucagon plays an antagonistic role to insulin in the regulation of glucose homeostasis, stimulating hepatic glucose release,[65] and therefore may contribute to the maintenance of the observed euglycemic conditions in the dual-rOoC system.

Next, the functionality of sc-liver organoids was analyzed. In the dual-rOoC chip, sc-liver organoids, when co-cultured with sc-islets, showed stable albumin and urea secretion at a level similar to sc-liver organoid mono-culture (Figure 5h). Sc-liver organoids in co-culture retained drug-dependent cytochromes P450 inducibility: CYP1A2 induction after treatment with Omeprazole, and CYP3A4 and CYP2C9 induction after treatment with Rifampicin (Figure 5i).

Finally, the cytokine status was analyzed under static, mono-culture, and co-culture conditions. Cytokine secretion is a sensitive marker of cellular stress and accompanies multiple pathological processes.[66–68] For instance, an increased expression of IL-8 and IL-6, as well as MCP-1 by pancreatic endocrine cells is seen during isolation and *in vitro* culture of human donor-derived islets.[69,70] A panel of cytokines and chemokines, that can be produced by islet under stress or disease conditions, was analyzed in static, mono-culture, and co-culture conditions in the sc-islet compartment after 14 days of culture.[70–72] Although the concentration of the tested cytokines in the medium was in general low, we observed a significantly higher level of the pro-inflammatory cytokine IL-8 and TNFα, as well as Interferon-gamma inducible protein-10 (IP-10) in multi-well static culture and *on-chip* mono-culture, than in co-culture (Figure 5k). In particular, a significant reduction of MCP-1 – a key factor for monocyte recruitment[73] – was observed in the co-culture *on-chip* (Figure 5i). Increased secretion of MCP-1 by β-cells is regulated by NF-κB pathway activation[74] and is associated with a poor outcome of islet allografts.[75] MCP-1 can also be produced by both hepatocytes[76] and hepatic stellate cells[77] (both present in sc-liver organoids) in response to pathogenic stimuli and has been shown to play an important role in the progression of liver injury.[78] Therefore, the decreased level of MCP-1 in the dual-rOoC platform additionally validates the beneficial effect of co-culturing sc-islets and sc-liver organoids *on-chip*.
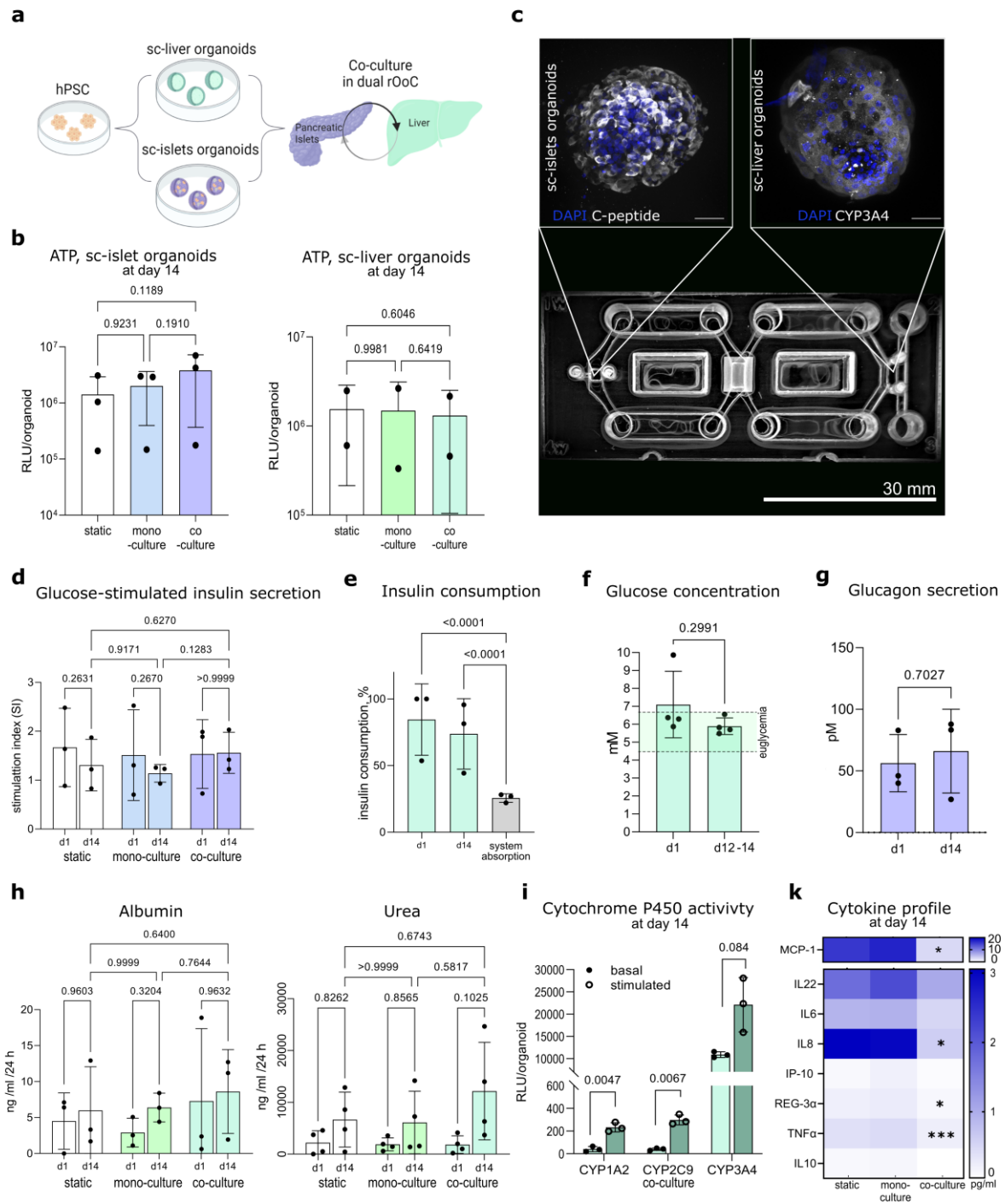
Figure 5. Coupling of sc-islets and sc-liver organoids on-chip. *a) Scheme of the experimental setup; b) Viability of sc-islet (left) and sc-liver organoids after 2 weeks of mono- and co-culture on the dual-rOoC, analyzed by ATP content (n = 3 and 2 independent experiments with N > 3 replicates in each). Significance was calculated using*

21

WILEY-VCH

paired one-way ANOVA test; c) Confocal on-chip imaging of sc-islet (left) and sc-liver organoids (right) stained with antibodies against C-peptide and CYP3A4 respectively. Scale bar = 50 µm; d) Insulin secretion by sc-islets measured during GSIS after 1 and 14 days of culture (n = 3 independent experiments, N > 3 replicates each). Significance was calculated using paired two-way ANOVA test; e) insulin consumption rate (R) by sc-liver organoids measured during GSIS after 1 and 14 days of culture (n = 3 independent experiments, N > 3 replicates each). Significance was calculated using a paired two-way ANOVA test; f) Glucose concentration in the background media after 24h incubation at the beginning and end of islets-liver co-culture in the dual-rOoC (n = 4 independent experiments, N > 3 replicates each). Significance was calculated using paired two-way ANOVA test; g) glucagon secretion by sc-islet organoids measured at 1 and 14 days of culture (n = 3 independent experiments, N > 3 replicates each). Significance was calculated using paired two-way ANOVA test; h) Albumin and urea secretion by sc-liver organoids in static conditions, mono- and co-culture on the dual-rOoC (n = 3 independent experiments, N > 3 replicates each). Significance was calculated using paired two-way ANOVA test; i) Cytochrome P450 (CYP) activity of sc-liver organoids after 2 weeks of co-culture on the dual-rOoC, represented as relative luminescence units (RLU), normalized to organoids number (n = 3 replicates). Significance is calculated by one-way ANOVA test; k) Heat map showing the absolute concentration of islets-relevant cytokines in the background media in the sc-islets compartment per 24 h after 14 days of sc-islet organoids culture under static conditions, in mono-culture and co-culture on the dual rOoC. (N = 5 replicates). Significance was calculated using an unpaired one-way ANOVA test. On-chip groups were compared to static condition, * p < 0.05, ** p < 0.01, *** p < 0.005.

Overall, the results indicate a functional islet-liver cross-talk in the dual-rOoC that was able to regulate glucose levels through insulin production by sc-islets and insulin-stimulated glucose uptake by sc-liver organoids. The measured tissue-specific functions of sc-islets and sc-liver organoids were preserved over 14 days in co-culture *on-chip*.

2.5. Mimicking obesity phenotype with sc-islet and sc-liver organoids on dual-rOoC

Obesity is a significant risk factor for T2DM and MASLD, profoundly affecting the cross-talk between metabolism-controlling organs,[7,79,80] whereby pathological immune reactions play a significant role in the progression of these interlinked metabolic disorders. To mimic obesity-inducing conditions *on-chip*, the co-culture medium for sc-islets and sc-liver organoids was supplemented with free fatty acids (saturated palmitic acid, and unsaturated –palmitic and oleic acids in a ratio 1:1, 250 µM each) and fructose (10 mM)[81] (Figure 6a) recapitulating overnutrition (referred as "obesity medium" below while organoids grown under these conditions *on-chip* were termed "obesity group"). The systemic effect of the obesity medium on the cross-talk between sc-islet and sc-liver organoids was studied using the dual-rOoC after 5 days of culture with daily media exchange.

First, changes in the morphology of sc-islets and sc-liver organoids that were induced by a 5-day exposure to an obesity medium were visualized *on-chip* with confocal imaging (Figure 6b). Under these conditions, the overall number of C-peptide-positive cells was reduced in sc-islets (Figure 6b, Figure S3a). As expected, obesity medium also led to substantial changes in

the sc-liver organoids. Similar to what was seen in mono-culture (Figure 4e), sc-liver organoids showed a significant accumulation of lipids in hepatocytes (Figure 6c, Figure S3b), marking the development of hepatic steatosis, the precursor stage of MASLD. Moreover, sc-liver organoids grown *on-chip* in an obesity medium were characterized by changes in the localization of the sterol regulatory element-binding transcription factor 1 (SREBP1) - a central transcription factor for insulin-regulated hepatic lipogenesis and cholesterol synthesis[82] (Figure S3c). In the untreated control group, SREBP1 was mostly localized in the perinuclear region indicating retention in the endoplasmic reticulum,[83] whereas in the obesity group, SREBP1 was evenly distributed in the cell cytoplasm, as well as abundantly present in the nuclei, indicating its activation (Figure 6c, Figure S3b). Standard functional tests of sc-liver organoids in the obesity group also exhibited a statistically significant decline of both albumin and urea secretion (Figure 6d), further showing signs of steatosis/MASLD.

Next, the glucose concentration was measured *on-chip* 24 h after medium replacement to a non-obesity co-culture medium for testing the ability of sc-liver organoids to regulate glucose levels (Figure 6e). The medium replacement was done in both control and obesity groups. While in the control group, sc-liver organoids consumed glucose to reach a euglycemic range between 5 and 7 mM, in the obesity group glucose concentrations were above 7 mM and in some cases exceeded 8 mM, representing a hyperglycemia-like condition.[84]

It was then tested how the co-culture system of control and obesity groups responded to glucose-stimulated insulin secretion in a standardized GSIS assay. A modest trend of decreased insulin secretion was observed in the obesity group that was, however, not statistically significant (Figure 6f). A modestly reduced GSIS index in the sc-islets of the obesity group was also seen (Figure 6f). Similar to the co-culture experiments under standard conditions, we calculated the insulin consumption R by the sc-liver organoids. For this, Eq. 7 was normed to the protein content (N) for both the IC and the LC:

$$R[\%] = 100 \cdot \left({}^{c_{islet} - c_{liver}}\!/\!_{c_{islet}} \right) \cdot \left({}^{N_{islet}}\!/\!_{N_{liver}} \right) \tag{8}$$

Within the liver circuit, we observed a statistically significant reduction of insulin consumption in the obesity group (Figure 6g). Reduced insulin consumption combined with increased glucose levels are early signs of insulin resistance in the sc-liver organoids. The glucagon level in the culture medium was not affected by the obesity medium (Figure S3d).

Thereafter, the mitochondrial metabolism of sc-islet and sc-liver organoids was tested in the control and obesity groups. Lactate is produced in anaerobic glycolysis and increased levels of lactate can indicate an impaired mitochondrial metabolism. Increased lactate levels have previously been reported in T2DM[85,86] and MASLD models.[87,88] Consistent with that, in the
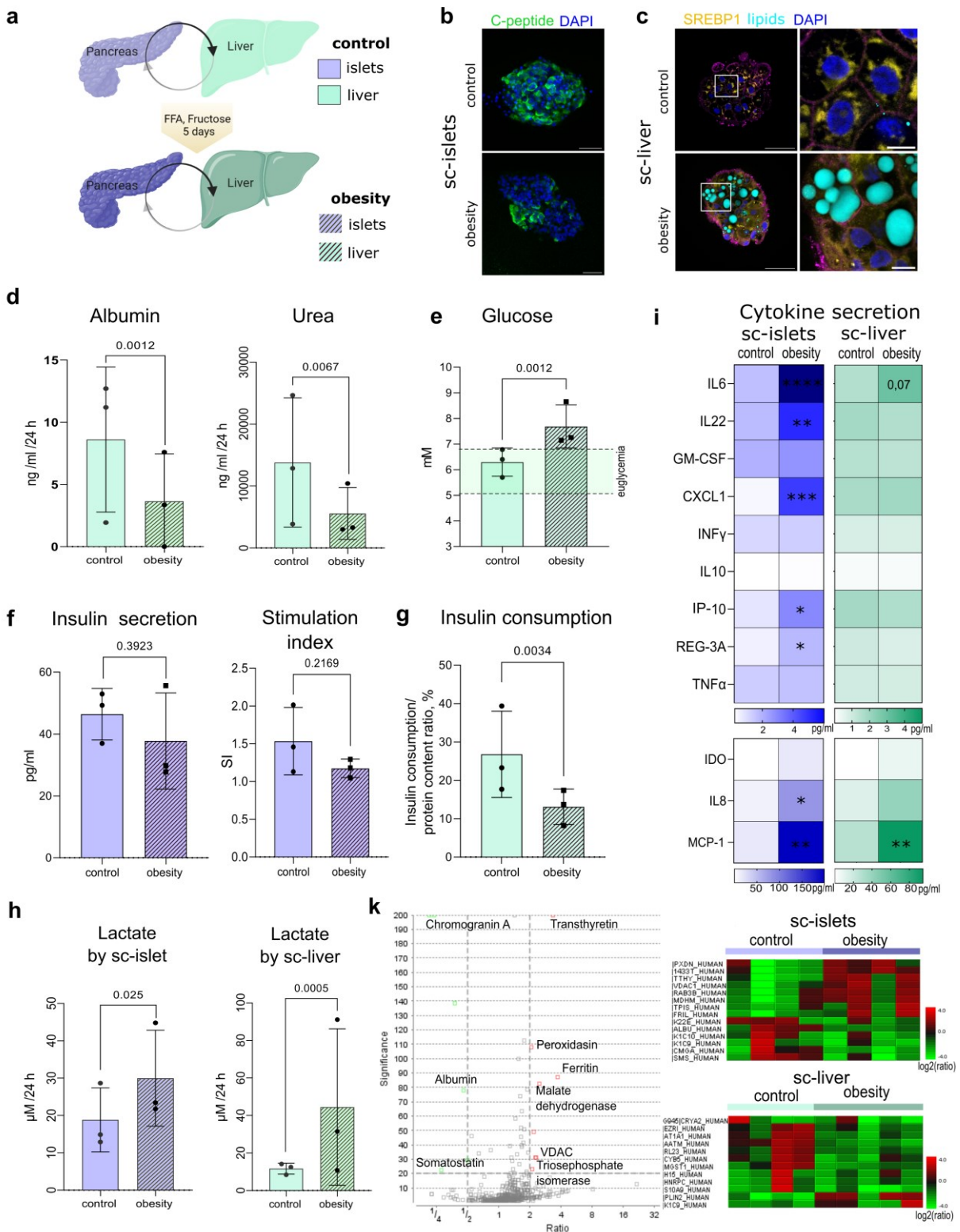
co-cultured sc-islets and sc-liver organoids, significantly increased levels of lactate were detected in the obesity group (Figure 6h).

To further characterize the sc-islet and sc-liver organoids in the control and obesity groups, we compared the secretion of cytokines in each compartment of the dual-rOoC platform (Figure 6i). This was possible since the exchange of proteins was delayed by the separating membrane. Hence, cytokine concentrations were measured in both sc-islets and sc-liver loops separately and normalized to the protein content of corresponding organoids. The most significant cytokine increase was detected for MCP-1 in both compartments, reflecting an elevated level of MCP-1 in the peripheral blood of patients with T2DM[89] and MASLD[90], as well as obesity.[91] Similarly, the concentration of the pro-inflammatory cytokine IL-6 was significantly increased in both compartments. Both MCP-1 and IL-6 have been reported to be secreted by islet and liver cells, affecting inflammation and leading to further metabolic disruptions.[90,92,93] The cytokines IL-22, CXCL1, IP-10, Reg-3A, and IL-8 were significantly increased in the IC of the obesity group, while they remained unaltered in the LC. TNF4α is another important cytokine implied in the onset and development of both T2DM and MASLD. However, no changes in TNF4α were observed between the control and obesity groups.

In addition, the proteome of sc-islet and sc-liver organoids in both control and obesity groups was compared. Despite a significant chip-to-chip variability originating from the small amount of biological material from the organoid samples, mass spectrometry-based proteomics revealed significant changes. In the sc-islets of the obesity group, a decrease of chromogranin A, somatostatin, and albumin, combined with an increase of transthyretin and ferritin was detected (Figure 6k). While the changes in insulin secretion were not statistically significant in the obesity group (Figure 6f), the proteomics data nevertheless are indicative of pre-diabetic changes. For instance, chromogranin A is expressed by endocrine cells and is essential for the biogenesis of secretory granules and for hormone secretion.[94,95] Somatostatin is secreted by δ-cells and is critical for the regulation of insulin secretion. Transthyretin is expressed in α-cells (glucagon secretin) which are increased in numbers in tissue samples from T2DM patients.[96] Similarly, increased levels of ferritin, an iron-binding protein, have been shown in T2DM patients. In the sc-liver organoids, the majority of proteins with altered levels of expression in the obesity group belong to proteins involved in mitochondrial metabolism and protein biosynthesis pathways. Furthermore, following lipid accumulation in sc-liver organoids in the obesity group, a significantly elevated level of perilipin, a lipid droplets-binding protein, was seen (Figure 6k).

Overall, the obtained results from the co-culture of sc-islets and sc-liver organoids under obesity conditions demonstrate the ability to model an emerging insulin resistance as well as a differential cytokine response *on-chip*.

Figure 6. Sc-islet and sc-liver organoids co-cultured on-chip in control and obesity medium. *a) Scheme of experimental setup; b) Representative confocal on-chip imaging of sc-islet organoids stained with antibodies against C-peptide and glucagon. Scale bar = 50 μm; c) Representative confocal on-chip imaging of sc-liver organoids stained with antibodies against SREBP1 and BODIPY™ 493/503. Scale bar = 50 μm; d) Albumin and urea secretion by sc-liver organoids (n = 3 independent experiments, N > 3 replicates in each). Significance was calculated by two-way ANOVA test; e) Glucose concentration in control and obesity groups after having been shifted to a 24-hour culture in basic medium (n = 3 independent experiments, N > 3 replicates in each). Significance was calculated by two-way ANOVA test; f) Insulin secretion by sc-islet organoids represented as*

GSIS index (left) and insulin concentration in high-glucose buffer (right) during GSIS assay, (n = 3 independent experiments, N > 3 replicates in each). Significance was calculated by two-way ANOVA test; g) Insulin consumption during GSIS by sc-liver organoids (n = 3 independent experiments, N > 3 replicates in each). Significance was calculated by two-way ANOVA test; h) Lactate production by sc-islets (left) and sc-liver organoids (right) (n = 3 independent experiments, N > 3 replicates in each). Significance was calculated by two-way ANOVA test; i) Heat map showing absolute concentration of cytokines in the sc-islet and sc-liver organoid compartments 24 hours after shifting from control and obesity conditions to basic media conditions (N = 5 replicates). Significance was calculated by unpaired one-way ANOVA test, * p < 0, 05, ** p < 0,01, *** p < 0,005; k) Proteomics analysis of sc-islet and sc-liver organoids in control and obesity groups. Left: volcano plot showing the changes in protein expression in sc-islets, represented as the ratio between the obesity and the low glucose group; right the most significantly up- and downregulated proteins in sc-islets and sc-liver organoids.

2.6. Anti-diabetic drug testing *on-chip*

Next, we explored the suitability of the platform for experimental drug testing. Three test compounds were selected: metformin, tolbutamide, and pyruvate kinase activator (TEPP46). Metformin is a commonly used glucose-lowering drug in T2DM with a spectrum of effects on multiple organs, including anti-inflammatory effects and beneficial effects in MASLD.[97] Tolbutamide belongs to the first generation of sulfonylureas and has been used as an oral hypoglycemic agent in T2DM therapy. However, it has largely been replaced by more effective medications such as metformin.[98] In particular, tolbutamide was replaced due to safety concerns as it is metabolized in the liver via CYP2C9 and may, in rare cases, induce liver injury. Pyruvate kinase activator is an experimental drug that has been shown to induce increased insulin release in preclinical T2DM models, as well as improved insulin sensitivity in steatosis and dyslipidemia in animal obesity models.[99]

Within the dual-rOoC, sc-islets and sc-liver organoids were cultured with an "obesity-inducing" medium as described above for five days (with daily media exchange). Next, the obesity medium was replaced with either a control medium (ObC group) or with a control medium supplemented with metformin (100 μM), tolbutamide (20 μM), or pyruvate kinase activator TEPP46 (10 μM). For the control group, sc-islets and sc-liver organoids were cultured in the control medium during the whole culture period.
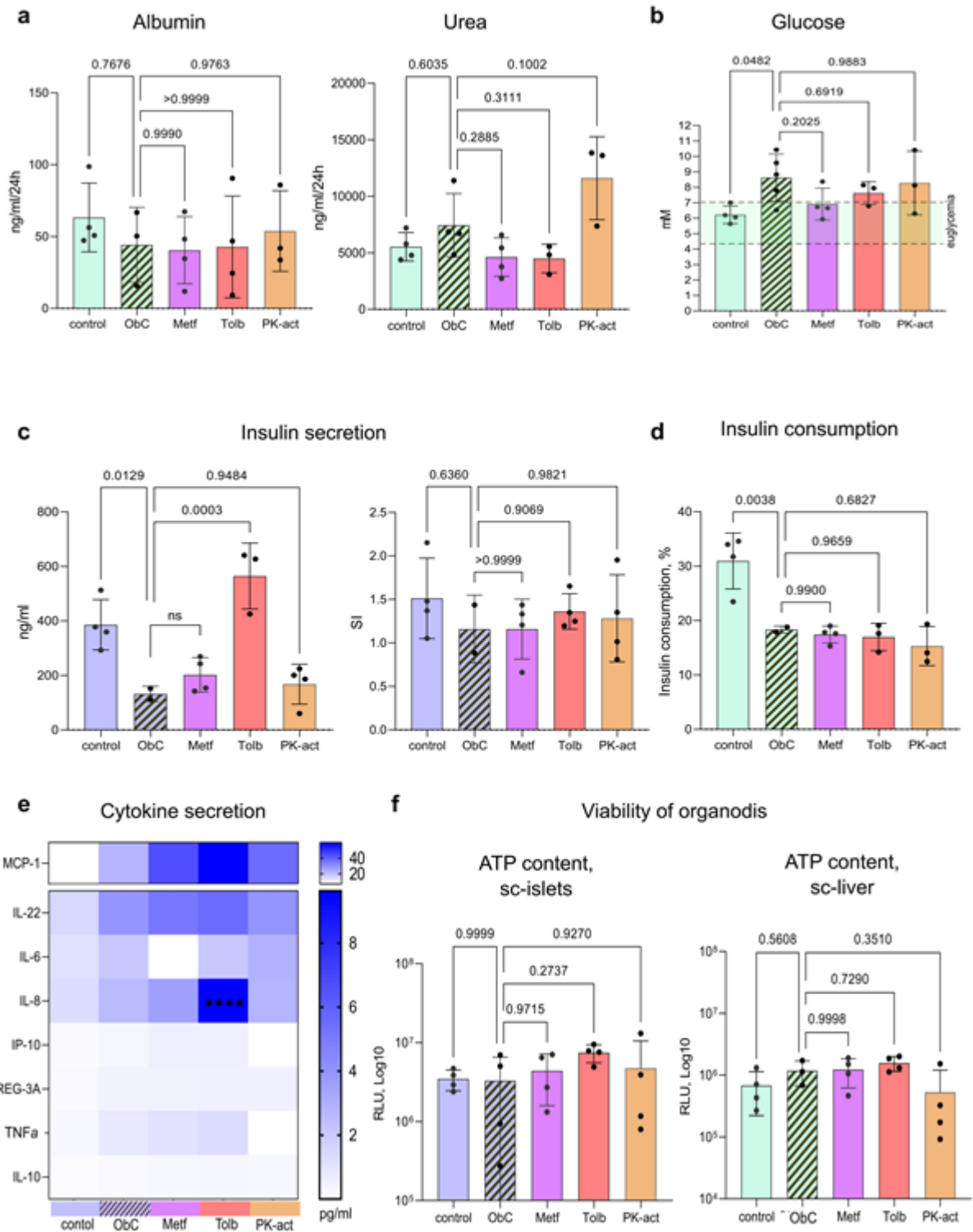
26

First, the samples were tested for indications of hepatotoxicity induced by the test drugs. This was done by measuring changes in albumin and urea production in the sc-liver organoids. None of the selected drugs had a statistically relevant negative effect on the markers (Figure 7a). Neither was a significant improvement of liver functions observed in any of the drug-treated groups, however, a trend of increased urea secretion was seen in the PK-act group.

Three days after replacing the obesity medium with the ObC control medium, glucose levels in the obesity group remained higher than in the non-obesity control group. The treatment with metformin led to a modest but not statistically relevant reduction of glucose levels without reaching the median euglycemic conditions of the non-obesity control group (Figure 7b).

Next, a GSIS assay was performed on the control and treatment groups after 3 days (of post-obesity) culture. Compared to obesity groups, a significant increase in insulin secretion by sc-islets was observed only in the tolbutamide-treated group. However, SI remained at a similar level for all groups (Figure 7c). This correlates well with previous preclinical and clinical studies for tolbutamide.[100,101] Metformin is known to decrease the hepatic glucose output and to increase the hepatic insulin sensitivity, however, without a direct effect on insulin secretion.[101] Therefore, the observed unaltered insulin secretion in response to metformin treatment *on-chip* also mirrors the clinical observation. Although the tested drugs were not efficient in restoring insulin consumption by sc-liver organoids, for which a longer treatment scheme may be needed, there was a trend of reduced glucose levels in the metformin-treated group (Figure 7d).

Since the cytokine profile has shown to be a sensitive indicator for the response of sc-islets and sc-liver organoids to changes in culture conditions (Figure 6i), a multiplex cytokine assay was performed on the non-obesity control group, obesity group (ObC group), and the drug-treated obesity groups (Figure 7e). Consistently with previously published pre-clinical[102] and clinical data,[103] we observed no IL-6 secretion in 3 out of 4 chips in the metformin group. This was in contrast to other drug-treated groups, as well as in the ObC group, where IL-6 was detected in all chips. There were no statistically significant changes in the secretion of other tested cytokines between the ObC and drugs-treated groups, except a statistically relevant elevated level of IL-8 in the tolbutamide group (Figure 7e). MCP-1 levels were increased in the ObC and all drug-treated groups compared to the control group (Figure 7e). Changes in insulin secretion and an absence of hepatotoxicity also corresponded to the end-point assay of ATP content in sc-islets and sc-liver organoids of all tested groups (Figure 7f).

Taken together, the positive correlation between preclinical and clinical data of the tested drugs, and data obtained on the dual-rOoC suggests that the platform is suitable for further preclinical exploration.

a Albumin, Urea

b Glucose

c Insulin secretion

d Insulin consumption

e Cytokine secretion

f Viability of organodis — ATP content, sc-islets; ATP content, sc-liver

WILEY-VCH

Figure 7. Anti-diabetic drug testing on-chip. *a) Albumin and urea secretion by sc-liver organoids in control and obesity groups after having been shifted to a 24-hour culture in control medium without drugs (ObC group) and with drugs (Metf, Tolb, PK-act groups) (N > 3 replicates). Significance was calculated by one-way ANOVA test; b) Glucose concentration in control and obesity groups after having been shifted to a 24 hour culture in control medium (ObC group) (N > 3 replicates). Significance was calculated by one-way ANOVA test; c) Insulin secretion by sc-islets represented as insulin concentration in the high-glucose buffer during GSIS assay (left) and SI (right), (N > 3 replicates). Significance was calculated by one-way ANOVA test; d) Insulin consumption during GSIS by sc-liver organoids (N > 3 replicates in each). Significance was calculated by one-way ANOVA test; e) Heat map showing an absolute concentration of cytokines in the sc-islet and sc-liver organoid compartments 24 hours after shifting from control and obesity conditions to ObC media conditions (N > 3 replicates). Drug-treated groups were compared to the ObC group. Significance was calculated by unpaired one-way ANOVA test, *** p < 0,005. Abbreviations: Metf: metformin-treated group, Tolb: tolbutamide-treated group, PK-act: PK-act-treated group.*

3. Discussion

Multi-organ *in vitro* models promise to provide tools for recapitulating human physiology, enhancing our understanding of disease development, and testing drug responses. For systemic disorders in energy metabolism, such as T2DM, obesity, and MASLD, the cross-talk between the pancreas and the liver plays a central role, calling for systems that allow modeling the islet-liver axis.

To establish a scalable *in vitro* model of the human islets-liver axis, we have developed a pump-less "dual-rOoC" layout that allows separating the perfusion of two different circuits each containing one or more organ compartments while still allowing for a molecular cross-talk between both circuits through a permeable membrane. The pump-less approach significantly improves the usability of a system because no external pumps and tubes are required while maintaining a high level of scalability and functionality. To the best of our knowledge, no comparable pump-less OoC system is at present described in the literature.

The multilayer fabrication method using thermoplastic films allows rapid prototyping of the fluidic layout and, compared to the commonly used poly-di-methyl-siloxane (PDMS), ensures relatively low absorbance of proteins and small molecules.[104] Nevertheless, rOoC chips show e.g. some insulin absorption (29 %) as recently confirmed by mass spectroscopic measurements.[49] Possible causes for this unspecific binding might be the employed membrane and the used ECM material in the OCs rather than the chip surface itself. However, adsorption to the chip should be further investigated. Nevertheless, as insulin adsorption was the same in each of the tested chips, we used the above adsorption value for calculating the overall insulin consumption in the chips.

In our earlier study, we already showed the possibility of tuning the flow rate and thus the shear stress that adherent cells in the fluidic channels are exposed to in the rOoC.[42] The same method

can be employed in the dual-rOoC to mimic different flow conditions in both circuits. This can be achieved either by changing the design and volume of the reservoirs, or PC dimensions in each circuit or by changing the driving conditions of the device (liquid volume in each circuit, rotation speed, or maximal tilt). Importantly, differential flow rates in the two circuits appear to support a directed mass transport such as the directional flow of proteins in the system. We measured the flow rate in both PCs under different conditions (see. Figure S4) and observed a difference in the flow-time curve on both the islet-PC and the liver-PC. A possible explanation for the difference is the asymmetry of the fluidic resistances on both sides of the liver circuit, which results in an increased backflow near the liver-PC and thus reduces the transported volume to the membrane on the liver side. Nonetheless, this difference in the flow rate seems to be beneficial to support a directed mass transport through the membrane from the islet to the liver circuit as insulin transport studies performed on empty chips indicate.

To explain this behavior, we developed a computational FEM model the insulin transport in the dual-rOoC. The model takes into account the transient flow behavior (measured by μPIV) and indeed, the pressure difference caused by the alternating actuation of both circuits, and the differences in the flow rate in both circuits seem to be the governing effect of the observed directionality of the insulin transport. The calculated results are in good alignment with the measured transport kinetics. Via regression, mass transport coefficients can be obtained. Given this model and the possibility of manipulating the flow conditions (via tilt, speed, and volume) on both sides, we can now predict the behavior of the system in terms of its transport capacity between both circuits. Moreover, the model can be applied to a variety of other molecules. We run the FEM model on glucose (diffusion coefficient: 6e-10 m^2 s^{-1}) and discovered an almost similar transport kinetics as with insulin (Figure S5). However, the mass transport coefficients calculated via regression are slightly higher compared to the insulin transport (0.27 and 0.18 respectively) because of the higher diffusion coefficient. These results indicate that the mass transport is mainly pressure-driven and thus can be influenced by tuning the driving conditions and chip geometry. Nevertheless, further experiments should be performed on different-sized molecules and different driving conditions to prove this statement. (Figure S5).

Although tissue models based on human donor material still represent the gold standard for functional and/or metabolic studies, hPSC-derived organoids start to resemble adult functionality and metabolic features thus rendering them suitable for disease modeling while offering better scalability and long-term stability in culture.[105] Throughout a series of improvements, we and others have obtained pluripotent stem cell-derived sc-islets[49,106,107] and sc-liver organoids[54,62,108–110] that approach adult metabolic maturity while exhibiting improved intra-batch stability.[54] The close to physiological maturity of the here used pluripotent stem cell-derived organoids is in particular documented by the relevant hormone

secretion and oxygen consumption by sc-islets when compared to adult benchmark islets, and by the albumin/urea production by sc-liver organoids when compared to adult PHHs. However, further improvements and standardization are needed as in particular seen by inter-batch variability between the experiments. This relates also to the organoid/chip interface where variations in the manual loading, leading to variations in the amount of sc-islet and sc-liver organoids in the chips (see Materials and Methods), reduce the predictive power of the current experimental setting.

Similar to previously published pump-driven micro-physiological systems for co-culturing islet and liver tissue representations,[34,36,37] we demonstrated stable viability and functionality of both organoid types in the dual-rOoC. A functional islets-liver cross-talk was established in the system, as indicated by the secretion of insulin by sc-islets organoids and its uptake by sc-liver organoids, enabling them to consume glucose from the medium and maintaining a glucose concentration in the microfluidic system that is in the range of physiological glucose concentrations (5-7 mм, euglycemia) (Figure 5e). Importantly, the hormone secretion by sc-islets into the microfluidic system was sufficient to support a functional sc-liver culture in a hormone-free medium *on-chip*. Considering the effective insulin consumption by sc-liver organoids in the co-culture system (Figure 4d), we can assume that the insulin secretion by sc-islets in the co-culture system was even higher than the measured insulin concentration *on-chip*. The decoupling effect measured by the different insulin transport kinetic (Figure 2f) only delays the mass transport but does not prevent the mixing of both circuits completely. A particularly noteworthy benefit of the co-culture of sc-islets and sc-liver organoids is the reduced secretion of IL-8, IP10, TNFα, and in particular MCP-1. The details of the functional cross-talk that led to this remarkable reduction call for further experimental exploration.

It is well known that obesity significantly affects the cross-talk between metabolism-controlling organs,[7,79,80] representing a major risk factor for developing T2DM and MASLD. To test obesity conditions *on-chip*, a medium supplemented with fatty acids (FAs) and fructose was used. The isolated effect of both FAs and fructose on liver and islet organoids has been explored in *in vitro* models,[111,112] however, to the best of our knowledge, not in the context of a islets-liver cross-talk *on-chip*. Previous studies have demonstrated that pancreatic islets can use free fatty acids as nutrients leading to an increased insulin secretion,[113,114] while a prolonged treatment with FA, although in significantly higher concentrations than in our study (1-2 mм vs 250 µм), can induce β-cells dysfunctions.[115,116] Treatment of liver organoids (both PSC-derived and PHH) with FAs induces hepatic steatosis or fatty liver – the initial stage of MASLD.[61,64] Fructose is commonly used as a sweetener in processed food and represents another abundant component of an unhealthy diet,[112] associated with metabolic dysfunctions.[117] Fructose is mostly metabolized in the liver, leading to increased glucose

output and lactate secretion via gluconeogenic and glycolytic pathways respectively. While fructose does not directly affect insulin secretion, it can synergize with glucose to amplify insulin release.[112]

The combination of FFA and fructose affected sc-liver organoids as expected, leading to increased lipid accumulation (Figure 6c), impaired insulin sensitivity (Figure 6g), and increased glucose output (Figure 6e) leading to hyperglycemia that corresponds to prediabetic conditions.[133] This is supported by the proteomics data on sc-islets organoids (Figure 6k) and by the cytokine secretion profile (Figure 6i) that are indicative for prediabetic changes, including decrease in expression of chromogranin A (necessary for hormones secretion), somatostatin (secreted by δ-cells; regulating insulin secretion), and corresponding increase of transthyretin (expressed in α-cells), which is similar to data derived from tissue samples from T2DM patients.[96] In contrast to previous studies on chronic hyperglycemia, which used significantly higher concentrations of glucose (11 mM,[38] 19 mM,[118,119] or 25 mM,[39] against glucose level above 7 mM in our study, achieved by hepatic glucose output), we did not observe a failure of β-cells or a significant decrease in insulin secretion in the sc-islets.

The impact of excessive nutrients and hyperglycemia on the release of the pro-inflammatory cytokines IL-6, IL-22, IP-10, and MCP-1 (Figure 6i) further supports a faithful disease modeling *on-chip*. For example, epidemiological studies have revealed that IL-6 is implicated in the chronic inflammation that accompanies conditions such as obesity and T2DM,[120,121] circulating IP-10 has been described as a biomarker for MASLD disease progression and subsequent T2DM development,[122] while MCP-1 plays a key role in insulin resistance and its complications such as diabetic nephropathy.[123]

Over the past decades, the interplay between cellular metabolism and immune reactions has become a focus area of many studies with immune-metabolism emerging as a novel research field.[124] However, relevant *in vitro* systems for this type of study are still limited. The pro-inflammatory cytokine response of the sc-islet and sc-liver organoids, combined with the possibility of tracking metabolism on the dual-rOoC platform may in the future be expanded to study immune-metabolism *on-chip*. This is in particular attractive as we have previously shown that the rOoC platform supports the culture of circulating immune cells. [42]

For evaluating the effect of selected anti-diabetic drugs (metformin, tolbutamide, and pyruvate kinase activator TEPP46) we used readouts from supernatant medium describing the functionality of both tissue representations: insulin, glucose, and urea concentration, as well as the release of cytokines. The obtained data partially correspond to the clinical and preclinical studies of the effect of tested drugs, further confirming the relevance of the presented model. The scalability of the platform allows that these parameters can in follow-up studies be

monitored repetitively, applying various schemes for obesity induction and variations in drug dosing, and hence providing dynamic profiles of drug-induced changes/improvements in the system with increased granularity. The platform can be further improved by the integration of sensors suitable for online monitoring of glucose, insulin, and oxygen levels.[125]

In summary, the developed scalable *on-chip* system enables the cross-talk and functional integration of islet and liver tissue representations. The platform provides a basis for further functional studies of obesity, T2DM, and MASLD *on-chip*, as well as for testing of potential therapeutic interventions.

4. Materials and methods

4.1. Device fabrication

The rOoC chips are made of several laser-cut PMMA sheets (Hesaglas®, Topacryl AG, Switzerland) thermally bonded together. First, each layer was designed in Autodesk Inventor® 2022 (Autodesk Inc., USA) and saved as individual DXF files for laser machining. All parts were laser-cut with a conventional CO_2 laser cutter (Beambox®, Flux Inc., Taiwan). The reservoir layer (6 mm) was cut with a power of 28W and a speed of 3 mm s^{-1}. Thin PMMA films (0.4-0.5 mm) containing the PCs and OCs were placed on an aluminum plate for better heat distribution and processed with a power of 7.2/8 W and a speed of 18/20 mm s^{-1} respectively.

After structuring, the films were cleaned in an ultrasonic bath (USC100T, VWR International, USA) for 15 min, sprayed with a nitrogen gun, and dried in an oven at 65 °C for 15 min. Next, the protective film on each layer was removed and the substrates were UV-activated using an Excimer lamp with a 172 nm emission wavelength (ExciJet172 55-130, Ushio GmbH, Germany). The distance to the lamp was adjusted to 1 mm and the substrates were exposed to a dose of 0.6 J cm^{-2}. Finally, the parts were aligned on an aluminum plate using alignment pins and transferred to a pneumatic hot press (AirPress-0302, Across International LLC, USA). For equal pressure distribution and control, cleanroom paper was put on top of the stack and an electronic pressure regulator (ITV1030, SMC Corporation, Japan) was used to control the bonding pressure. After UV activation, PMMA can be thermally bonded below its glass transition temperature (T_g = 100 °C). We used a bonding pressure of 4 MPa, a temperature of 82 °C (top) & 67 °C (bottom), and a bonding time of 15 min.

The track-etched polycarbonate membrane (pore size: 3 µm, type: TSTP04700 Isopore™, Merck Millipore Ltd., Ireland) was manually cut into quadratic pieces (25 mm^2) and sandwiched (without prior UV treatment) between the layer 3 and 4. The whole rOoC was

bonded in one step. For *on-chip* confocal imaging, the devices were sealed with a 175-μm thick PMMA film (Merck Sigma, USA).

4.2. Flow measurement

The flow was measured by micro-particle image velocimetry (μPIV) with a setup as described earlier.[47] As tracers, dyed 10-μm polystyrene microparticles (Merck Sigma, USA) in a concentration between 0.1 % and 1 % (m/v) were used. Images were acquired in transmission by using a 3.3x Macro Zoom Lens (Edmund Optics Ltd., UK) coupled with a high-speed camera (acA1300-200uc, Basler AG, Germany). The digital microscope was mounted to a customized stand including an LED backlight illumination .[42] Particle movement was observed in a field of view of 592 × 100 Px (1 Px = 6.09 μm) at 2270 fps and 100 μs acquisition time. Later, image stacks of approx. 45,000 frames (20 s recording time) were evaluated using an optical flow algorithm previously applied to calculate the motion of beating cardiomyocytes.[126] The setup is suitable for detecting flow velocities up to 100 mm s^{-1}.

According to Eq. 2, the μPIV setup needs to be calibrated to a known flow rate. We obtain the calibration factor k via linear regression given the transported volume and the volume filled in the reservoirs:

$$k = \frac{\int Q \, dt}{V_{res}} \approx 1.84 \tag{9}$$

Due to a possible interaction between both PCs, we blocked one side of the chip to obtain a flow only within one PC (bidirectional flow) with the whole liquid transported from one reservoir to the other. For calibration (see Suppl. Material) a reservoir volume between 75 and 125 μL, a rotation speed of 3 rpm, and a tilt of 18 ° were used. The calculated factor is equivalent to the one obtained in the previous study.

In the previous paper we have already proven that the used tracer particles do follow the flow to a good extent by calculating by calculating the relaxation time of the dispersed particles to $\tau \approx 7.3 \mu s$.[42] That means, the tracers need roughly 40 μs after a sudden change in the velocity to adapt to the new velocity (tracing error < 0.5 % for a decay function of $e^{-\frac{t}{\tau}}$). This value is much lower than the recording frequency of 2270 fps thus it can be stated that the particles follow the flow to a good extent.

Membrane transport model

Permeability k, is a property of porous media characterizing their ability to transmit fluids through, and it was defined in the present model as follows:[127]

$$k = \frac{\mu L P}{\pi r^2 R_{pore}}$$

(10)

With μ [Pa s] representing the dynamic viscosity of media, L [m] the length of the porous medium, P its porosity, r [m] the pore radius, R_{pore} [kg m^{-4} s^{-1}] the pore resistance. On the other hand, to define pore resistance, and consider the medium as being a thin, porous membrane, Dagan's equation is used to account for the entrance/exit effect of flow through a short through pore. Therefore, pore resistance, for a single pore, was expressed as follows:[128]

$$R_{pore} = \frac{\mu}{r^3}\left[3 + \frac{8}{\pi}\left(\frac{L}{r}\right)\right]$$

(11)

Moreover, the *Transport of Diluted Species* module was used to simulate the motion of diluted molecules flowing within the bulk media. As it results from the combined effect of advection and diffusion, the molecule transport was solved by engaging the Advection-Diffusion equation (Eq. 1). However, the presence of a porous membrane, with a certain degree of tortuosity, τ, requires further characterization, to fully define the transport of molecules across the respective interface. For such, the Millington and Quirk model was employed, defining effective diffusivity, D_{eff} [m^2 s^{-1}], in the porous membrane as follows:

$$D_{eff} = \frac{P}{\tau} D$$

(12)

4.3. Generation of stem cell-derived liver organoids

Human embryonic stem cells (H1, Coriell Institute for Medical Research) and human induced pluripotent stem cells (HLC_1: WTC-11, Coriell Institute for Medical Research; HLC_2: WTSIi013-A Wellcome Trust Sanger Institute) were routinely cultured in mTeSR media (StemCell Technologies, catalog no. 85857) human E8 media (Thermo Fisher Scientific, catalog no. A1517001) correspondingly, on plates coated with 0.1 % (v/v) Geltrex (Thermo Fisher Scientific, catalog no. A1413201) in a humidified 37 °C, 5 % CO$_2$ incubator. The pluripotency of cells before differentiation was confirmed by flow cytometry, qPCR, and immunofluorescent imaging for pluripotency markers. Normal karyotype and absence of mycoplasma contamination were confirmed for all used cell lines.

Hepatic differentiation was performed using a modification of previously published protocols.[53] Briefly, iPSC/ESCs were differentiated toward definitive endoderm in IMDM/F12 media containing 1 % (v/v) lipid concentrate (Thermo Fisher Scientific, catalog no. 11905031), 100 μg mL^{-1}transferrin, 3 μм CHIR99021 (Tocris Bioscience, catalog no. 4423), 50 nм PI-103 (Tocris Bioscience, catalog no. 2930) and 100 ng mL^{-1} activin A (Peprotech, catalog no. 120-14P) for 24 h and 100 ng mL^{-1} activin A for subsequent 48 h. The definitive endoderm cells were treated with 10 ng mL^{-1} FGF2 (Peprotech, catalog no. 100-18B) and 20 ng mL^{-1} BMP4 (Peprotech, catalog no. 120-05) in IMDM/F12 medium supplemented with 1 % (v/v) N-2 (Thermo Fisher Scientific, catalog no. 17502-048), 1 % (v/v) B-27 minus vitamin A (Thermo Fisher Scientific, catalog no. 12587010) and 1 % (v/v) lipid concentrate, then with 5 μм A8301 (Stem Cell Technologies, catalog no. 72022), 20 ng mL^{-1} HGF (Peprotech, catalog no. 100-39H), 20 ng mL^{-1} BMP4, 1 % (v/v) B-27 with vitamin A for 3 more days and with 25 ng mL^{-1} HGF, 1 % (v/v) DMSO for another 5 days. At day 12, cells were detached by accutase and aggregated in the agarose U bottom microwells in the presence of 25 ng mL^{-1} HGF, 0.1 μм Dexamethasone, 10 μм Y-27632, 0.5 % (v/v) ITS, 0.1 % (v/v) lipids concentrate, 100 μм Ascorbic acid-2 phosphate (AAP), 1 % (v/v) B-27 (without vitamin A) and 1 % (v/v) N-2. After the formation of spheroids at day 13, media was replaced with William's E media, supplemented with 5 % (v/v) FBS, 20 ng ml^{-1} HGF, and 10 ng ml^{-1} oncostatin M (Peprotech, catalog no. 300-10), 1 % (v/v) ITS, 100 μм AAP, 0.1 μм Dexamethasone. For further maturation, organoids were cultured in microwells in William's E media, supplemented with 1 % (v/v) ITS, 0.1 μм Dexamethasone, 20 ng ml^{-1} Oncostatin M and 1 % (v/v) MEM Non-Essential Amino Acids Solution (NEAA, Thermo Fisher Scientific, catalog no. 11140050), 10 μм DAPT for another 10 days with the replacement of media every 48 h.

4.4. Generation of stem cell-derived pancreatic sc-islets

SC-islets were generated from human pluripotent cell line H1. Undifferentiated H1 cells were cultured in Essential 8™ Medium on tissue culture plates coated with Geltrex (Thermo Fisher Scientific, catalog no. A1413201) in a humidified incubator containing 5 % CO_2 at 37 °C. To initiate differentiation towards sc-islets, undifferentiated cells were seeded as single cells at 2×10^5 cells cm^{-2} in 1:50 diluted Geltrex™ coated cell culture plates. 24 hours after seeding, cells were washed with PBS and incubated with stage 1 media supplemented 3 μм CHIR99021 (Selleckchem, catalog no. S2924) and 100 ng mL^{-1} Activin A (PeproTech, catalog no. 120-14) for 1 day, then stage 1 basal media supplemented with 100 ng mL^{-1} Activin A for next 3 days. At stage 2, the cells were incubated with stage 1 basal media supplemented with 0.255 mм vitamin C (Sigma, catalog no. A4544), 1.25 μм IWP2 (Bio-Techne, catalog no. 3533), and 50 ng mL^{-1} KGF (PeproTech, catalog no. AF-100-19) for 2 days. At stage 3, the cells were

incubated with stage 3 basal media supplemented with 0.2 μM LDN193189 (Tocris, catalog no. 6053), 0.2 μM TPPB (MedChemExpress, catalog no. HY-12359), 2 μM Retinoid Acid (R2625, Sigma), 0.25 μM SANT1 (Sigma, catalog no. C23H27N5) and 50 ng mL^{-1} KGF for 2 days. At stage 4, the cells were incubated with stage 3 basal media supplemented with 0.1 μM Retinoid Acid, 0.25 μM SANT1, 0.2 μM LDN193189, 0.2 μM TPPB and 50 ng mL^{-1} KGF for 4 days. On the first day of stage 5, the cells were incubated with stage 5 basal media supplemented with 0.1 μM Retinoid Acid, 0.25 μM SANT1, 0.2 μM LDN193189, 10 μM ALK5 inhibitor II (Enzo Life Sciences, catalog no. ALX-270-445-M005), 1 μM T3 (Sigma, catalog no. T6397), 1 μM Xxi (Sigma, catalog no. 565789) and 1 μM Latrunculin A (Bio-Techne, catalog no. 3973). The cell media were then changed every day for the following 6 days at stage 5 without Latrunculin A added. During the first 7 days of stage 6, the cells were cultured in an enriched serum-free medium (ESFM) with media change every day. At day 7 of stage 6, the cells were dissociated with TrypLE EExpress (Gibco, catalog no. 12604013) and seeded at 1×10^6 cells mL^{-1} in an ultra-low attachment cell culture plate from Corning (Sigma, catalog no. CLS3261). The cells were then aggregated and maintained as spheroids on an orbit-shaker (Thermo Fisher) at 100 rpm for over 7 days till analysis, the media was changed every other day. The basal media were as follows. Stage 1 basal media: MCDB 131 (Invitrogen, catalog no. 10372-019) additionally supplemented with 1 % P/S, 100x GlutaMAX (Invitrogen, catalog no. 35050079), 0.5 % BSA (Proliant, catalog no. 68700), 1.174 g L^{-1} sodium bicarbonate (Sigma, catalog no. S6297), 4.5 mM glucose (Sigma, catalog no. G7021). Stage 3 basal media: MCDB 131 additionally supplemented with 1 % P/S, 100x GlutaMAX, 2 % BSA, 1.154g L^{-1} sodium bicarbonate, 4.5 mM glucose, and 0.25 mM vitamin C. Stage 5 basal media: MCDB 131 additionally supplemented with 1 % P/S, 1x GlutaMAX, 2 % BSA, 1.154g L^{-1} sodium bicarbonate, 14.5 mM glucose, 0.25 mM vitamin C, 10 μg mL^{-1} Heparin (Sigma, catalogue no. H3149) and 200x ITS-X (ThermoFisher, catalogue no. 51500056). ESFM: MCDB 131 additionally supplemented with 1 % P/S, 1 % GlutaMAX, 100x NEAA, 2 % BSA, 1000x Trace Elements A (25-021-CI, Corning),1000x Trace Elements B (25-022-CI, Corning), and 10 μM ZnSO4 (Z0251, Sigma).

4.5. Co-culture *on-chip*

Sc-liver organoids and sc-islet organoids were co-cultured in separate compartments of the dual-rOoC (see Figure 1a, Figure S2a). For this, 3 to 9 sc-islets organoids and 5 to 15 sc-liver organoids in 5 μL of basal medium were mixed with 15 μL Geltrex (Thermo Fisher Scientific, catalog no. A1413201) on ice. Organoids in the Geltrex mixture were immediately loaded in corresponding chambers and placed for 3 minutes in a humidified 37 °C, 5 % CO$_2$ to polymerize the hydrogel. After that, 450 μL, 375 μL, and 75 μL of the co-culture medium were added to the islet-PC, the liver-PC, and the liver drainage channel respectively. The co-culture

medium consisted of a mixture of William's E medium and MCDB 131 in ratio 1:1 (v/v) supplemented with 0.1 % (v/v) Trace Elements A (25-021-CI, Corning), 0.1 % (v/v) Trace Elements B (25-022-CI, Corning), 0.1 % (v/v) NEAA (Thermo Fisher Scientific, catalog no. 11140050), 1 % (v/v) Glutamax, 0,1% (w/v) BSA (Proliant, catalog no. 68700) and 10 μM ZnSO4 (Z0251, Sigma). The medium was exchanged every 24 hours with conditioned medium being collected and stored at -80⁰C for the required assays.

4.6. Obesity induction and drug treatment

The obesity condition was induced *on chip* after 5 days of co-culture of sc-islets and sc-liver organoids in standard conditions by supplementing the basal medium, described above, with 250 μM saturated palmitic acid (Sigma, catalog no. P5585), 250 μM unsaturated oleic acid (Sigma, catalog no. O1383) and 10 mM fructose (Sigma, catalog no. F3510). This medium is referred to as "obesity medium" throughout the article. The organoids were grown in the obesity medium for 5 days before further analyses. The obesity medium was exchanged every 24 hours.

Drug treatment was performed after 5 days of obesity induction. For this, obesity medium was exchanged with standard basal medium supplemented with metformin (Selleckchem, catalog no. S5958, 10 μM), tolbutamide (Selleckchem, catalog no. S2443, 10 μM), or pyruvate kinase inhibitor TEPP-46 (Medchem Express, catalog no. HY-18657, 10 μM). The medium was changed every 24 hours and the total duration of the drug treatment was 3 days.

4.7. Oxygen consumption rate analysis

The oxygen consumption rate (OCR) analysis was performed with a Seahorse XFe24 analyzer (Agilent). First, 30 differentiated sc-islets or primary human islets were hand-picked and seeded in 24-well cell culture microplates and washed 3 times with RPMI-1640 media (Sigma, catalog no. R6504), and then incubated with RPMI-1640 media supplemented with 0.1 % BSA and 2 mM glucose for two hours, at 37 ˚C. The base respiration rate was determined using an assay media containing 2 mM glucose. The calibration was performed for 5 cycles with a 6 min interval. Next, the cells were incubated in a media with 20 mM glucose to determine the OCR change upon high glucose stimulation. The oxygen consumption at 20 mM glucose was measured for 6 cycles and 6 min intervals. OIligomycin A (Cell Signaling Technology, catalog no. 9996L), CCCP (Carbonyl cyanide 388 3-chlorophenylhydrazone, Sigma, catalog no. C2920), Rotenone (Sigma, catalog no. R8875) and Antimycin A (Sigma, catalog no. A8674) in a concentration of 5 μM were added sequentially. The oxygen consumption rate was then measured for 5 cycles with a 6 min interval. The OCR values were normalized to the averaged baseline values obtained during calibration.

4.8. LIVE/DEAD imaging and viability assay

ATP content was evaluated using Cell Titer-Glo® 3D Cell Viability Assay (Promega, Sweden) according to the manufacturer's instructions.

4.9. Glucose-stimulated insulin and glucagon secretion

30 sc-islets were hand-picked into Transwell cell culture inserts (Sigma, catalog no. CLS3414), and placed into 24-well cell culture plates. The cells were washed three times and equilibrated in Krebs-Ringer buffer (KRB: 128 mM NaCl, 5 mM KCl, 2.7 mM CaCl$_2$, 1.2 mM MgSO$_4$, 1 mM Na$_2$HPO$_4$, 1.2 mM KH$_2$PO$_4$, 5 mM NaHCO$_3$, 10 mM HEPES and 0.1 % BSA) with 2 mM glucose for 1 hour at 37 ˚C. The sc-islets were then incubated sequentially in KRB containing 2 mM (Low), 20 mM (High), 2 mM (Low) glucose, and 2 mM glucose with 30 mM KCl for 60 min each. The supernatant was collected after each step of incubating. Insulin was determined by using a human insulin ELISA kit (Mercodia, catalog no. 10-1113-10), and glucagon was determined by using a human glucagon ELISA kit (Mercodia, catalog no. 10-1271-01).

4.10. Glucose level assay

The glucose concentration in the supernatant media was evaluated using a Glucose Colorimetric Detection Kit (Invitrogen™, catalog no. EIAGLUC) following the manufacturer's instructions.

4.11. Cytokine assay

Cytokine and chemokine secretion in the supernatant media was evaluated using ProcartaPlex Immunoassay 12 Plex (ThermoFisher Scientific, assay ID MXGZF7U) following the manufacturer's instructions. The analyte concentrations were then normalized to total protein content, using Pierce™ BCA Protein Assay Kit (Thermo Fisher Scientific) according to the vendor's instruction.

4.12. Albumin and Urea production assays

Albumin content in the supernatant media was evaluated using the Human Albumin ELISA Quantitation Set (Bethyl Laboratories, catalog no. E88-129). The concentration of urea in the medium was quantified calorimetrically using a urea assay kit (BioAssay Systems, DIUR-100), following the manufacturer's instructions. Both albumin and urea concentration was normalized to the total protein content, using Pierce™ BCA Protein Assay Kit (Thermo Fisher Scientific, catalog no. A53227) according to the vendor's instruction.

4.13. Cytochrome CYP3A4 activity

Cytochrome CYP3A4 enzymatic activity of HLCs was measured using P450-Glo™ Assay with Luciferin-IPA (catalog no. V9001, Promega, Sweden). The relative luminescence was normalized to total protein content, measured by Pierce™ BCA Protein Assay Kit (Thermo Fisher Scientific, catalog no. A53227) according to the vendor's instruction.

4.14. Immunofluorescence staining and microscopy of sc-liver organoids

Cell cultures in rOoC were fixed in 4 % (w/v) PFA for 20 min on an orbital shaker. Each step was followed by three washing steps (each 10 min using orbital shaking) in DPBS. Permeabilization and blocking were performed by incubation in PBS with 1% (m/v) BSA (Sigma Aldrich), 0.2 % (v/v) Triton-X100 (Sigma Aldrich), and 0.5 % (v/v) DMSO at RT for 2 h on the orbital shaker. Staining with primary antibodies was performed for 24 h (at 4 °C) with subsequently 2 h incubation with secondary antibodies (Jackson ImmunoResearch, West Grove, PA) diluted with 1 % BSA, 0.1 % Triton-X100 in PBS. Primary antibodies (Ab) used in this study: rabbit polyclonal Ab to human serum albumin (Abcam, catalog no. ab2406, 1:400), goat polyclonal antibody to E-cadherin (R&D systems, catalog no. AF748-SP, 1:250), mouse monoclonal Ab to CYP3A4 (3H8) (Invitrogen, catalog no. MA5-17064, 1:250), rabbit polyclonal to VE-Cadherin (Abcam, catalog no. ab33168, 1:400), goat polyclonal Ab to PDGFR beta (R&D systems, catalog no. AF385, 1:50), rabbit polyclonal Ab to SREBP1 (Novus Biologicals, catalog no. NB100-2215, 1:400). Secondary Ab used in this study: Alexa Fluor® 488 AffiniPure Donkey Anti-Goat IgG (H+L) (catalog no. 705-545-147, 1:300), Cy™3 AffiniPure Donkey Anti-Rabbit IgG (H+L) (catalog no. 711-165-152, 1:400), Alexa Fluor® 647 AffiniPure Donkey Anti-Mouse IgG (H+L) (catalog no. 715-605-150, 1:400) (all secondary Ab are from Jackson ImmunoResearch). Lipids staining was performed using BODIPY™ 493/503 (Thermo Fisher Scientific, catalog no. D3922)   Nuclear counterstaining was performed with 1 µg/mL Hoechst 33258 (Sigma Aldrich). Confocal microscopy was performed on a Zeiss 700 laser scanning confocal microscope using standard filter sets and laser lines with a 40x oil immersion objective. Images were acquired using Zen software (Zeiss) as Z-stacks with 2 µм spacing between stacks. The confocal images were analyzed using Fiji software[13] and are displayed as a resulting Z-stack.

SREBP1 intensity and lipids content from confocal images were quantified using Python script (Supplementary 6). Masks for the cytoplasm, nuclei, and lipids were computed for every image of the stack by thresholding. The threshold values were kept the same for the whole dataset as the imaging conditions were similar. Cytoplasm masks inside holes were filled out and the lipid mask was subtracted from it. The mean values of SREBP present in the obtained cell masks and in the nuclei were computed for further analysis. Every third stack was used in the analysis.

4.15. Immunofluorescence staining and microscopy of sc-islet organoids

Sc-islets at stage 6 (between 7-14 days of culture) were harvested and fixed in 4 % (w/v) PFA for 30 min at 4°C. After blocking with PBS with 1 % (m/v) BSA (Sigma Aldrich), 0.2 % (v/v) Triton-X100 (Sigma Aldrich) for 30 mins, the cells were washed with PBS with 1 % (m/v) BSA (Sigma Aldrich) and placed in 30% sucrose (Sigma Aldrich) overnight at 4°C. The cells were then embedded in O.C.T (Fisher Scientific) and preserved at -80 °C until sectioning. For cryosectioning, the sc-islets were cut into 10 μm thick slides. Following antibodies were used for Immunofluorescence staining, rabbit anti-CHGA (Novus Biologicals, catalog no. NB120–15160, 1:500), rabbit anti-human MAFA (Abcam, catalog no. NB120–15160, 1:100), mouse anti-Nkx-6.1 (University of Iowa, DHB, catalog no. F55A12-S, 1:100), rat anti-insulin/C-peptide (University of Iowa, DHB, catalog no. GN-ID4-s, 1:200), mouse anti-human somatostatin (Santa Cruz, catalog no. sc-55565, 1:500), mouse Anti-Glucagon (Sigma, catalog no. G2654, 1:800). C-peptide positive cell numbers from confocal images were quantified using Python script (Supplementary 6).

4.16. Substrate oxidation assay

The radioactive substrate oxidation assay was performed to evaluate glucose and oleic acid metabolism as previously described.[129] On the day of analysis, the media was supplemented with D-[^{14}C(U)]glucose (0.5 μCi mL^{-1}, 200 μM) or [1-^{14}C]oleic acid (OA) (0.5 μCi mL^{-1}, 100 μM) (PerkinElmer NEN®, catalog no. NEC042A001MC and NEC317250UC, respectively) and 100 nM insulin (NovoNordisk, Actrapid®Penfill® 100IE mL^{-1}) was added or not. In parallel, a 96-well UniFilter® microplate (PerkinElmer NEN®, catalog no. 6055090) was activated for the capture of CO_2 by the addition of 1 M NaOH, mounted on top of the ultra-low attachment U-bottom 96-well plate (Thermo Fisher Scientific, catalog no. 174927). Next, cells were incubated for 4 h using the modified media to trap radioactive CO_2. Afterward, the organoids were washed in PBS and harvested in 0.1 M NaOH. The $^{14}CO_2$ trapped in the filter and cell-associated (CA) radioactivity was measured by the addition of a scintillation fluid (Ultima Gold XR, PerkinElmer, catalog no. 6013111) and counted on a 2450 MicroBeta2 scintillation counter (PerkinElmer, catalog no. 2450-0020). All results were adjusted for protein content, measured by the Bio-Rad protein assay (Bio-Rad, catalog no. 5000001) using a VICTOR™ Nivo X4 Multilabel Plate Reader (PerkinElmer, catalog no. HH35000500).

Cellular uptake was calculated as the sum of $^{14}CO_2$ and CA radioactivity measurements: CO_2+CA. Fractional oxidation was calculated as CO_2/uptake.

4.17. RNA extraction and real-time polymerase chain reaction (PCR)

RNA was isolated using an RNeasy Micro kit (Qiagen, Germany) according to the manufacturer's protocol. cDNA was synthesized using a High-Capacity cDNA Reverse

Transcription Kit (Thermo Fisher Scientific, catalog no. 4368814). Gene expression analysis was performed using a TaqMan Universal mix on a TaqMan ViiA7 Real-Time PCR System. The primers used in this study are listed in Supplementary 7, all purchased from ThermoFisher Scientific. *TBP, GAPDH,* and *RPL* genes were used as endogenous controls. The levels of expression of genes of interest were quantified by the ddCt method with normalization to corresponding primary human cells: primary human hepatocytes and islets from 3 donors each, LSEC – from 1 donor, and HSC – from 2 donors.

4.18. Proteomics

Organoid samples (6-19 organoids) were pooled and suspended in 200 µL ice-cold Dulbecco's phosphate-buffered saline, followed by centrifugation at 10.000 g for 10 min at 4 °C. The supernatant was discarded, and the organoids were prepared for proteomic analysis following the protocol for Sample Preparation by Easy Extraction and Digestion (SPEED) with minor modifications.[130] The organoids were lysed in neat trifluoroacetic acid (TFA), in a 1:4 ratio (sample:TFA). The protein concentration in samples was estimated after the addition of TFA, using NanoDrop (ThermoFisher Scientific) to measure absorbance at 280 nm after mixing 1 µL of a sample with 4 µL type-1 water. The rest of the sample was neutralized by adding 2 м Tris base in a volume ten times the volume of TFA. DL-dithiothreitol (DTT) and iodoacetamide (IAM) replaced Tris(2-carboxyethyl)phosphine and 2-choloroacetamide from the original protocol as reducing and alkylating reagents. DTT was added to a final concentration of 10 mм and incubated at 700 rpm at 56 °C for 25 min, followed by the addition of IAM to a final concentration of 20 mм and incubation at 700 rpm at room temperature and in the dark for 30 min. To quench the alkylation, 5 mм DTT was added and incubated at 700 rpm at room temperature for 15 min. The samples were diluted 1:5 with water, and trypsin was added in the ratio of 50:1 (substrate : trypsin) and incubated at 700 rpm at 37 °C for 16 hours. TFA was added to a final concentration of 2 % and the samples were reduced to app. half volume using a SpeedVac (ThermoFisher Scientific).

The samples were desalted using an Omix tip with C18 material embedded in the tip. The Omix Tip was conditioned with 30 µL 0.1 % TFA in 50 % acetonitrile and equilibrated with 30 µL 0.1 % TFA in water (both 3 x 10 µL aliquots). The samples were loaded by slowly pipetting 10 µL at once, repeated 10 times, followed by a wash with 0.1 % TFA in water (3 x 10 µL). Peptides were eluted with 10 µL 0.1 % TFA in 50 % acetonitrile. Eluate was dried using a SpeedVac at 30 °C and reconstituted with 5 µL 0.1 % formic acid.

The samples were analyzed by LC-MS using a nanoElute nanoflow LC system coupled via a nanoelectrospray ionization source, using a CaptiveSpray emitter (Inner diameter (ID) 20 µм) to a timsTOF Pro (Bruker, Bremen, Germany). The capillary voltage was 1.5 kV. Mobile phase A was 0.1 % FA in water and mobile phase B was 0.1 % FA in ACN. Peptides were separated on an Aurora Ultimate C18 column (15cm x 75 µм ID, 1.7 µм particles, Ion Opticks, Fitzroy,

Austria) using a gradient from 2-35 % B over 60 min with a flow rate of 200 nL min^{-1}. The column temperature was 50 °C. MS acquisition was performed in DDA-PASEF mode, with a mass range of 100 to 1700 m z^{-1}. The number of PASEF ranges was set to 20 with a total cycle time of 1.16 s, charge up to 5, target intensity of 20000, intensity threshold of 1750, and active exclusion with release after 0.4 min. An inversed reduced TIMS mobility (1/k0) of 0.85-1.40 Vs cm^{-2} was used with a range time of 100 ms, an accumulation time of 100 ms, a duty cycle of 100 %, and a ramp rate of 9.51 Hz. Precursors for DDA were fragmented with an ion mobility-dependent collision energy, which was linearly increased from 20 to 59 eV. Proteomics data were analyzed using PEAKS Studio X Pro software (Bioinformatics Solution Inc).

4.19. Statistics

Statistical analyses and graph generation were performed using GraphPad PRISM 9 (GraphPad Software Inc.). Long-term culture on-chip and obesity modeling was performed on three independent experiments (sc-islets and sc-liver organoids from three independent differentiations) with at least three microfluidic devices per group. Data sets with n > 3 were tested for normality using Shapiro-Wilk test. If at least one of groups failed the normality test, nonparametric Mann–Whitney U test or one way ANOVA on ranks (Kruskal-Wallis test) were used. To account for the variability between devices originating from the variation in the number of organoids loaded in the chip, as well as differentiation batch-to-batch variation, the two-way ANOVA analysis was applied. A two-tailed, t-test (for comparison of two groups) and one-way ANOVA analysis (for comparison of more than two groups) were applied for the comparison of sc-derived organoids to primary donor material, and for analysis of drug response. The correction for the multiple comparison was performed using post-hoc tests: the Tukey method for the comparison of mean with every other mean, and Dunnett's - to compare every mean with control groups. The data are presented as mean ± SD. Statistical significance was assigned as not significant (NS) $P > 0.05$; or significant with *$p \leq 0.05$; **$p \leq 0.01$; ***$p \leq 0.001$; ****$p \leq 0.0001$.

Author Contributions

A.A. designed the biological part of the paper, performed cell experiments, prepared figures, and wrote the paper together with M.B., C.W., and S.K. Cell experiments were performed by A.A. and C.W. with the assistance of I.W. and J.S.. A.A., C.W., S.A., J.S, and I.W. performed gene expression, imaging and functional assays for characterization of sc-organoids and on-chip culture. A.D.F performed the radioactive substrate oxidation assays. T.C. performed confocal image analysis. Microdevices were fabricated by A.G. M.B. developed the technology, designed and characterized the devices, prepared figures, and wrote the technical and modeling part of the paper. P. D. M. performed the membrane modeling in Comsol. J.M. and H.R-L. performed the proteomics assay. S.K. and H.S. supervised the work, provided

laboratory space, and procured funding for this study. All authors have read and agreed to the published version of the manuscript.

Conflicts of Interest

M.B., A.A., and S.K. have applied for a patent covering the main principle of fluid actuation and application and are planning to commercialize the technology.

Ethical Statement

The ethical approval for this project including the use of primary islets is covered under REK 50786.

Literature

[1] M. E. Rinella, J. V. Lazarus, V. Ratziu, S. M. Francque, A. J. Sanyal, F. Kanwal, D. Romero, M. F. Abdelmalek, Q. M. Anstee, J. P. Arab, et al., *J. Hepatol.* **2023**, DOI 10.1016/j.jhep.2023.06.003.

[2] J. M. Paik, P. Golabi, Y. Younossi, M. Srishord, A. Mishra, Z. M. Younossi, *Hepatol. Commun.* **2020**, *4*, 1769.

[3] D. J. Magliano, E. J. Boyko, IDF Diabetes Atlas 10th edition scientific committee, *IDF DIABETES ATLAS*, International Diabetes Federation, Brussels, **2021**.

[4] T. G. Cotter, M. Rinella, *Gastroenterology* **2020**, *158*, 1851.

[5] T. Lobstein, H. Brinsden, M. Neveux, **2022**.

WILEY-VCH

[6]   S. Soltanieh, M. Salavatizadeh, H. Poustchi, Z. Yari, A. Mansour, M. E. Khamseh, M. Malek, F. Alaei-Shahmiri, A. Hekmatdoost, *Heliyon* **2023**, *9*, e13983.

[7]   Z. Liu, Y. Zhang, S. Graham, X. Wang, D. Cai, M. Huang, R. Pique-Regi, X. C. Dong, Y. E. Chen, C. Willer, et al., *J. Hepatol.* **2020**, *73*, 263.

[8]   E. Muzurović, D. P. Mikhailidis, C. Mantzoros, *Metabolism.* **2021**, *119*, 154770.

[9]   L. López-Bermudo, A. Luque-Sierra, D. Maya-Miles, R. Gallego-Durán, J. Ampuero, M. Romero-Gómez, G. Berná, F. Martín, *Front. Endocrinol.* **2022**, *13*.

[10]   J. E. Campbell, C. B. Newgard, *Nat. Rev. Mol. Cell Biol.* **2021**, *22*, 142.

[11]   K. F. Leavens, M. J. Birnbaum, *Crit. Rev. Biochem. Mol. Biol.* **2011**, *46*, 200.

[12]   Y. Hayashi, *J. Diabetes Investig.* **2021**, *12*, 32.

[13]   A. R. Cox, O. Barrandon, E. P. Cai, J. S. Rios, J. Chavez, C. W. Bonnyman, C. J. Lam, P. Yi, D. A. Melton, J. A. Kushner, *PloS One* **2016**, *11*, e0159276.

[14]   F. Gerst, R. Wagner, G. Kaiser, M. Panse, M. Heni, J. Machann, M. N. Bongers, T. Sartorius, B. Sipos, F. Fend, et al., *Diabetologia* **2017**, *60*, 2240.

[15]   J. S. Hansen, S. Rutti, C. Arous, J. O. Clemmesen, N. H. Secher, A. Drescher, C. Gonelle-Gispert, P. A. Halban, B. K. Pedersen, C. Weigert, et al., *J. Clin. Endocrinol. Metab.* **2016**, *101*, 550.

[16]   A. Rajwani, V. Ezzat, J. Smith, N. Y. Yuldasheva, E. R. Duncan, M. Gage, R. M. Cubbon, M. B. Kahn, H. Imrie, A. Abbas, et al., *Diabetes* **2012**, *61*, 915.

[17]   D. R. Clemmons, *J. Mol. Endocrinol.* **2018**, *61*, T139.

[18]   R. Palma, A. Pronio, M. Romeo, F. Scognamiglio, L. Ventriglia, V. M. Ormando, A. Lamazza, S. Pontone, A. Federico, M. Dallio, *J. Clin. Med.* **2022**, *11*, 3649.

[19]   X. Chen, J. Xiao, J. Pang, S. Chen, Q. Wang, W. Ling, *Nutrients* **2021**, *13*, 3139.

[20]   M. A. Moh Moh, C.-H. Jung, B. Lee, D. Choi, B.-Y. Kim, C.-H. Kim, S.-K. Kang, J.-O. Mok, *Diab. Vasc. Dis. Res.* **2019**, *16*, 186.

[21]   K. Rehman, M. S. H. Akash, *J. Biomed. Sci.* **2016**, *23*, 87.

[22]   A. Ogata, A. Morishima, T. Hirano, Y. Hishitani, K. Hagihara, Y. Shima, M. Narazaki, T. Tanaka, *Ann. Rheum. Dis.* **2011**, *70*, 1164.

[23] S. J. Burke, D. Lu, T. E. Sparer, M. D. Karlstad, J. J. Collier, *Mol. Immunol.* **2014**, *62*, 54.

[24] J. J. Swaroop, D. Rajarajeswari, J. N. Naidu, *Indian J. Med. Res.* **2012**, *135*, 127.

[25] G. S. Hotamisligil, N. S. Shargill, B. M. Spiegelman, *Science* **1993**, *259*, 87.

[26] L. Piemonti, B. E. Leone, R. Nano, A. Saccani, P. Monti, P. Maffi, G. Bianchi, A. Sica, G. Peri, R. Melzi, et al., *Diabetes* **2002**, *51*, 55.

[27] G. Yoshimatsu, F. Kunnathodi, P. B. Saravanan, R. Shahbazov, C. Chang, C. M. Darden, S. Zurawski, G. Boyuk, M. A. Kanak, M. F. Levy, et al., *Diabetes* **2017**, *66*, 2857.

[28] K. Khunti, L. Ji, J. Medina, F. Surmont, M. Kosiborod, *Diabetes Obes. Metab.* **2019**, *21*, 2349.

[29] R. Sawangjit, B. Chongmelaxme, P. Phisalprapa, S. Saokaew, A. Thakkinstian, K. V. Kowdley, N. Chaiyakunapruk, *Medicine (Baltimore)* **2016**, *95*, e4529.

[30] Y. Takahashi, Y. Soejima, T. Fukusato, *World J. Gastroenterol. WJG* **2012**, *18*, 2300.

[31] C. P. D. Kottaisamy, D. S. Raj, V. Prasanth Kumar, U. Sankaran, *Lab. Anim. Res.* **2021**, *37*, 23.

[32] Y. R. Im, H. Hunter, D. de Gracia Hahn, A. Duret, Q. Cheah, J. Dong, M. Fairey, C. Hjalmarsson, A. Li, H. K. Lim, et al., *Hepatology* **2021**, *74*, 1884.

[33] J.-Y. Shoji, R. P. Davis, C. L. Mummery, S. Krauss, *Adv. Healthc. Mater.* **2023**, e2301067.

[34] B. S. Beydag-Tasöz, S. Yennek, A. Grapin-Botton, *Nat. Rev. Endocrinol.* **2023**, *19*, 232.

[35] D. E. Ingber, *Nat. Rev. Genet.* **2022**, *23*, 467.

[36] S. Bauer, C. Wennberg Huldt, K. P. Kanebratt, I. Durieux, D. Gunne, S. Andersson, L. Ewart, W. G. Haynes, I. Maschmeyer, A. Winter, et al., *Sci. Rep.* **2017**, *7*, 14620.

[37] B. Casas, L. Vilén, S. Bauer, K. P. Kanebratt, C. W. Huldt, L. Magnusson, U. Marx, T. B. Andersson, P. Gennemark, G. Cedersund, *PLOS Comput. Biol.* **2022**, *18*, e1010587.

[38]   R. Zandi Shafagh, S. Youhanna, J. Keulen, J. X. Shen, N. Taebnia, L. C. Preiss, K. Klein, F. A. Büttner, M. Bergqvist, W. van der Wijngaart, et al., *Adv. Sci.* **2022**, *9*, 2203368.

[39]   T. Tao, P. Deng, Y. Wang, X. Zhang, Y. Guo, W. Chen, J. Qin, *Adv. Sci.* **2022**, *9*, 2103495.

[40]   M. Busek, A. Aizenshtadt, M. Amirola-Martinez, L. Delon, S. Krauss, *Biosensors* **2022**, *12*, 126.

[41]   C. Olsen, C. Wang, S. Abadpour, E. Lundanes, A. S. Hansen, F. S. Skottvoll, H. Scholz, S. R. Wilson, *J. Chromatogr. B Analyt. Technol. Biomed. Life. Sci.* **2023**, *1215*, 123577.

[42]   M. Busek, A. Aizenshtadt, T. Koch, A. Frank, L. Delon, M. A. Martinez, A. Golovin, C. Dumas, J. Stokowiec, S. Gruenzner, et al., *Lab. Chip* **2022**, DOI 10.1039/D2LC00919F.

[44]   M. Busek, S. Nøvik, A. Aizenshtadt, M. Amirola-Martinez, T. Combriat, S. Grünzner, S. Krauss, *Biosensors* **2021**, *11*, 162.

[48]   G. K. Batchelor, *An Introduction to Fluid Dynamics*, Cambridge University Press, Cambridge, **2000**.

[49]   C. Olsen, C. Wang, A. Aizenshtadt, S. Abadpour, E. Lundanes, F. S. Skottvoll, A. Golovin, M. Busek, S. Krauss, H. Scholz, et al., *ELECTROPHORESIS* **n.d.**, *n/a*, DOI 10.1002/elps.202300095.

[50]   A. E. Schaffer, B. L. Taylor, J. R. Benthuysen, J. Liu, F. Thorel, W. Yuan, Y. Jiao, K. H. Kaestner, P. L. Herrera, M. A. Magnuson, et al., *PLOS Genet.* **2013**, *9*, e1003274.

[51]   S. R. Jesinkey, A. K. Madiraju, T. C. Alves, O. H. Yarborough, R. L. Cardone, X. Zhao, Y. Parsaei, A. R. Nasiri, G. Butrico, X. Liu, et al., *Cell Rep.* **2019**, *28*, 759.

[52]   J. C. Davis, T. C. Alves, A. Helman, J. C. Chen, J. H. Kenty, R. L. Cardone, D. R. Liu, R. G. Kibbey, D. A. Melton, *Cell Rep.* **2020**, *31*, 107623.

[54]   V. LaLone, A. Aizenshtadt, J. Goertz, F. S. Skottvoll, M. B. Mota, J. You, X. Zhao, H. E. Berg, J. Stokowiec, M. Yu, et al., *Cell Rep. Methods* **2023**, *3*, 100440.

[55]   K. S. Kømurcu, I. Wilhelmsen, J. L. Thorne, S. Krauss, S. R. Wilson, A. Aizenshtadt, H. Røberg-Larsen, *J. Steroid Biochem. Mol. Biol.* **2023**, *232*, 106355.

[56] A. Fatehullah, S. H. Tan, N. Barker, *Nat. Cell Biol.* **2016**, *18*, 246.

[57] L. Magomedova, C. L. Cummins, in *Metab. Control* (Ed: S. Herzig), Springer International Publishing, Cham, **2016**, pp. 73–93.

[58] C. Beaupere, A. Liboz, B. Fève, B. Blondeau, G. Guillemain, *Int. J. Mol. Sci.* **2021**, *22*, 623.

[59] L. T. Ang, A. K. Y. Tan, M. I. Autio, S. H. Goh, S. H. Choo, K. L. Lee, J. Tan, B. Pan, J. J. H. Lee, J. J. Lum, et al., *Cell Rep.* **2018**, *22*, 2190.

[60] S. J. Mun, J.-S. Ryu, M.-O. Lee, Y. S. Son, S. J. Oh, H.-S. Cho, M.-Y. Son, D.-S. Kim, S. J. Kim, H. J. Yoo, et al., *J. Hepatol.* **2019**, *71*, 970.

[61] R. Ouchi, S. Togo, M. Kimura, T. Shinozawa, M. Koido, H. Koike, W. Thompson, R. A. Karns, C. N. Mayhew, P. S. McGrath, et al., *Cell Metab.* **2019**, *30*, 374.

[62] M. Kimura, T. Iguchi, K. Iwasawa, A. Dunn, W. L. Thompson, Y. Yoneyama, P. Chaturvedi, A. M. Zorn, M. Wintzinger, M. Quattrocelli, et al., *Cell* **2022**, *185*, 4216.

[63] C. C. Bell, D. F. G. Hendriks, S. M. L. Moro, E. Ellis, J. Walsh, A. Renblom, L. Fredriksson Puigvert, A. C. A. Dankers, F. Jacobs, J. Snoeys, et al., *Sci. Rep.* **2016**, *6*, 25187.

[64] M. Kozyra, I. Johansson, Å. Nordling, S. Ullah, V. M. Lauschke, M. Ingelman-Sundberg, *Sci. Rep.* **2018**, *8*, 14297.

[65] I. Quesada, E. Tudurí, C. Ripoll, A. Nadal, *J. Endocrinol.* **2008**, *199*, 5.

[66] W. Huang, L. J. Hickson, A. Eirin, J. L. Kirkland, L. O. Lerman, *Nat. Rev. Nephrol.* **2022**, *18*, 611.

[67] H. J. Forman, H. Zhang, *Nat. Rev. Drug Discov.* **2021**, *20*, 689.

[68] S. Muralidharan, P. Mandrekar, *J. Leukoc. Biol.* **2013**, *94*, 1167.

[69] U. Johansson, A. Olsson, S. Gabrielsson, B. Nilsson, O. Korsgren, *Biochem. Biophys. Res. Commun.* **2003**, *308*, 474.

[70] S. Negi, A. Jetha, R. Aikin, C. Hasilo, R. Sladek, S. Paraskevas, *PLOS ONE* **2012**, *7*, e30415.

[71] Z. Zhou, M.-J. Xu, B. Gao, *Cell. Mol. Immunol.* **2016**, *13*, 301.

[72]   M. Y. Donath, M. Böni-Schnetzler, H. Ellingsgaard, P. A. Halban, J. A. Ehses, *Trends Endocrinol. Metab.* **2010**, *21*, 261.

[73]   S. L. Deshmane, S. Kremlev, S. Amini, B. E. Sawaya, *J. Interferon Cytokine Res. Off. J. Int. Soc. Interferon Cytokine Res.* **2009**, *29*, 313.

[74]   B. Kutlu, M. I. Darville, A. K. Cardozo, D. L. Eizirik, *Diabetes* **2003**, *52*, 348.

[75]   R. Melzi, A. Mercalli, V. Sordi, E. Cantarelli, R. Nano, P. Maffi, G. Sitia, L. G. Guidotti, A. Secchi, E. Bonifacio, et al., *Cell Transplant.* **2010**, *19*, 1031.

[76]   J. Kang, J. Postigo-Fernandez, K. Kim, C. Zhu, J. Yu, M. Meroni, B. Mayfield, A. Bartolomé, D. H. Dapito, A. W. Ferrante, et al., *JCI Insight* **2023**, *8*, DOI 10.1172/jci.insight.165369.

[77]   S. Xi, X. Zheng, X. Li, Y. Jiang, Y. Wu, J. Gong, Y. Jie, Z. Li, J. Cao, L. Sha, et al., *Front. Med.* **2021**, *8*.

[78]   P. Mandrekar, A. Ambade, A. Lim, G. Szabo, D. Catalano, *Hepatol. Baltim. Md* **2011**, *54*, 2185.

[79]   A. Chobot, K. Górowska-Kowolik, M. Sokołowska, P. Jarosz-Chobot, *Diabetes Metab. Res. Rev.* **2018**, *34*, e3042.

[80]   J. V. Lazarus, H. E. Mark, Q. M. Anstee, J. P. Arab, R. L. Batterham, L. Castera, H. Cortez-Pinto, J. Crespo, K. Cusi, M. A. Dirac, et al., *Nat. Rev. Gastroenterol. Hepatol.* **2022**, *19*, 60.

[81]   L. Tappy, *J. Exp. Biol.* **2018**, *221*, jeb164202.

[82]   H. Shimano, R. Sato, *Nat. Rev. Endocrinol.* **2017**, *13*, 710.

[83]   Y. Gong, J. N. Lee, P. C. W. Lee, J. L. Goldstein, M. S. Brown, J. Ye, *Cell Metab.* **2006**, *3*, 15.

[84]   E. S. Moghissi, M. T. Korytkowski, M. DiNardo, D. Einhorn, R. Hellman, I. B. Hirsch, S. E. Inzucchi, F. Ismail-Beigi, M. S. Kirkman, G. E. Umpierrez, et al., *Diabetes Care* **2009**, *32*, 1119.

[85]   J. Aleksandar, P. Vladan, S. Markovic-Jovanovic, R. Stolic, J. Mitic, T. Smilic, *J. Diabetes Res.* **2016**, *2016*, e6901345.

[86] S. O. Crawford, R. C. Hoogeveen, F. L. Brancati, B. C. Astor, C. M. Ballantyne, M. I. Schmidt, J. H. Young, *Int. J. Epidemiol.* **2010**, *39*, 1647.

[87] S. C. Kalhan, L. Guo, J. Edmison, S. Dasarathy, A. J. McCullough, R. W. Hanson, M. Milburn, *Metabolism.* **2011**, *60*, 404.

[88] N. Cabré, F. Luciano-Mateo, G. Baiges-Gayà, S. Fernández-Arroyo, E. Rodríguez-Tomàs, A. Hernández-Aguilera, M. París, F. Sabench, D. Del Castillo, J. López-Miranda, et al., *Aliment. Pharmacol. Ther.* **2020**, *51*, 374.

[89] G. Daniele, R. Guardado Mendoza, D. Winnier, T. V. Fiorentino, Z. Pengou, J. Cornell, F. Andreozzi, C. Jenkinson, E. Cersosimo, M. Federici, et al., *Acta Diabetol.* **2014**, *51*, 123.

[90] X. Pan, A. Chiwanda Kaminga, A. Liu, S. W. Wen, J. Chen, J. Luo, *Front. Immunol.* **2020**, *11*.

[91] R. C. Parish, S. Todman, S. K. Jain, *Metab. Syndr. Relat. Disord.* **2016**, *14*, 291.

[92] J. R. Weaver, J. J. Odanga, E. K. Breathwaite, M. L. Treadwell, A. C. Murchinson, G. Walters, D. P. Fuentes, J. B. Lee, *Diabetes Metab. Res. Rev.* **2021**, *37*, e3405.

[93] M.-C. Chen, P. Proost, C. Gysemans, C. Mathieu, D. L. Eizirik, *Diabetologia* **2001**, *44*, 325.

[94] T. Kim, J.-H. Tao-Cheng, L. E. Eiden, Y. P. Loh, *Cell* **2001**, *106*, 499.

[95] G. M. Portela-Gomes, J. R. Gayen, L. Grimelius, M. Stridsberg, S. K. Mahata, *Regul. Pept.* **2008**, *151*, 19.

[96] G. T. Westermark, P. Westermark, *Exp. Diabetes Res.* **2008**, *2008*, 429274.

[97] Y. Geng, Z. Wang, X. Xu, X. Sun, X. Dong, Y. Luo, X. Sun, *Transl. Res.* **2023**, DOI 10.1016/j.trsl.2023.08.001.

[98] R. A. Costello, S. Nicolas, A. Shivkumar, in *StatPearls*, StatPearls Publishing, Treasure Island (FL), **2023**.

[99] A. Abulizi, R. L. Cardone, R. Stark, S. L. Lewandowski, X. Zhao, J. Hillion, L. Ma, R. Sehgal, T. C. Alves, C. Thomas, et al., *Cell Metab.* **2020**, *32*, 751.

[100] S. Kadowaki, T. Taminato, T. Chiba, M. Nozawa, T. Fujita, A. W. Norman, *Endocrinology* **1983**, *112*, 2187.

[101] R. S. Vardanyan, V. J. Hruby, in *Synth. Essent. Drugs* (Eds: R. S. Vardanyan, V. J. Hruby), Elsevier, Amsterdam, **2006**, pp. 343–348.

[102] Y. Jing, F. Wu, D. Li, L. Yang, Q. Li, R. Li, *Mol. Cell. Endocrinol.* **2018**, *461*, 256.

[103] E. Fidan, H. Onder Ersoz, M. Yilmaz, H. Yilmaz, M. Kocak, C. Karahan, C. Erem, *Acta Diabetol.* **2011**, *48*, 297.

[104] T. E. Winkler, A. Herland, *ACS Appl. Mater. Interfaces* **2021**, *13*, 45161.

[105] A. Marsee, F. J. M. Roos, M. M. A. Verstegen, HPB Organoid Consortium, H. Gehart, E. de Koning, F. Lemaigre, S. J. Forbes, W. C. Peng, M. Huch, et al., *Cell Stem Cell* **2021**, *28*, 816.

[106] N. J. Hogrebe, P. Augsornworawat, K. G. Maxwell, L. Velazco-Cruz, J. R. Millman, *Nat. Biotechnol.* **2020**, *38*, 460.

[107] D. Balboa, T. Barsby, V. Lithovius, J. Saarimäki-Vire, M. Omar-Hmeadi, O. Dyachok, H. Montaser, P.-E. Lund, M. Yang, H. Ibrahim, et al., *Nat. Biotechnol.* **2022**, *40*, 1042.

[108] D. Hendriks, J. F. Brouwers, K. Hamer, M. H. Geurts, L. Luciana, S. Massalini, C. López-Iglesias, P. J. Peters, M. J. Rodríguez-Colman, S. Chuva de Sousa Lopes, et al., *Nat. Biotechnol.* **2023**, DOI 10.1038/s41587-023-01680-4.

[109] S. Kogler, A. Aizenshtadt, S. Harrison, F. S. Skottvoll, H. E. Berg, S. Abadpour, H. Scholz, G. Sullivan, B. Thiede, E. Lundanes, et al., *Anal. Chem.* **2022**, *94*, 17677.

[110] A. Aizenshtadt, L. Midtøy, B. Thiede, S. Krauss, H. Reberg-Larsen, S. Wilson, *LCGC Suppl.* **2023**, *36*, 16.

[111] E. A. Vilas-Boas, D. C. Almeida, L. P. Roma, F. Ortis, A. R. Carpinelli, *Cells* **2021**, *10*, 3328.

[112] M. R. Laughlin, *Nutrients* **2014**, *6*, 3117.

[113] Y. Itoh, S. Hinuma, *Hepatol. Res.* **2005**, *33*, 171.

[114] C. Warnotte, P. Gilon, M. Nenquin, J.-C. Henquin, *Diabetes* **1994**, *43*, 703.

[115] C. J. Nolan, M. S. R. Madiraju, V. Delghingaro-Augusto, M.-L. Peyot, M. Prentki, *Diabetes* **2006**, *55*, S16.

WILEY-VCH

[116] Y. Itoh, Y. Kawamata, M. Harada, M. Kobayashi, R. Fujii, S. Fukusumi, K. Ogi, M. Hosoya, Y. Tanaka, H. Uejima, et al., *Nature* **2003**, *422*, 173.

[117] L. Tappy, K.-A. Lê, *Physiol. Rev.* **2010**, *90*, 23.

[118] E. Hall, M. Dekker Nitert, P. Volkov, S. Malmgren, H. Mulder, K. Bacos, C. Ling, *Mol. Cell. Endocrinol.* **2018**, *472*, 57.

[119] E. Ottosson-Laakso, U. Krus, P. Storm, R. B. Prasad, N. Oskolkov, E. Ahlqvist, J. Fadista, O. Hansson, L. Groop, P. Vikman, *Diabetes* **2017**, *66*, 3013.

[120] L. L. Lehrskov, R. H. Christensen, *Semin. Immunopathol.* **2019**, *41*, 491.

[121] B. K. Pedersen, M. A. Febbraio, *Nat. Rev. Endocrinol.* **2012**, *8*, 457.

[122] C.-C. Chang, C.-L. Wu, W.-W. Su, K.-L. Shih, D.-C. Tarng, C.-T. Chou, T.-Y. Chen, C.-T. Kor, H.-M. Wu, *Sci. Rep.* **2015**, *5*, 10096.

[123] F. G. Scurt, J. Menne, S. Brandt, A. Bernhardt, P. R. Mertens, H. Haller, C. Chatzikyrkou, *Diabetes Metab. Res. Rev.* **2022**, *38*, e3497.

[124] G. S. Hotamisligil, *Immunity* **2017**, *47*, 406.

[125] G. A. Clarke, B. X. Hartse, A. E. Niaraki Asli, M. Taghavimehr, N. Hashemi, M. Abbasi Shirsavar, R. Montazami, N. Alimoradi, V. Nasirian, L. J. Ouedraogo, et al., *Sensors* **2021**, *21*, 1367.

[127] P. Loskill, T. Sezhian, K. Tharp, F. T. Lee-Montiel, S. Jeeawoody, W. M. Reese, P.-J. H. Zushin, A. Stahl, K. E. Healy, *Lab. Chip* **2017**, *17*, 1645.

[128] H. H. Chung, M. Mireles, B. J. Kwarta, T. R. Gaborski, *Lab. Chip* **2018**, *18*, 1671.

[129] A. J. Wensaas, A. C. Rustan, K. Lövstedt, B. Kull, S. Wikström, C. A. Drevon, S. Hallén, *J. Lipid Res.* **2007**, *48*, 961.

[130] J. Doellinger, A. Schneider, M. Hoeller, P. Lasch, *Mol. Cell. Proteomics MCP* **2020**, *19*, 209.
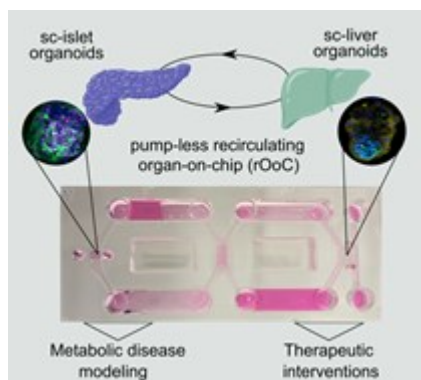
WILEY-VCH

Table of Contents:

Pump-Less, Recirculating Organ-On-Chip (rOoC) Platform To Model The Metabolic Crosstalk Between Islets And Liver.

The current study presents a novel dual pump-less recirculating Organ-on-Chip (dual-rOoC) platform designed for studying type 2 diabetes, obesity, and metabolic liver disease. It replicates metabolic interactions between the liver and pancreatic islets using human stem cell-derived organoids, and allows improved disease modelling and drug testing.